

Source Parameters of Intermediate-Depth Vrancea (Romania) Earthquakes from Empirical Green's Functions Modeling

by

Adrien Oth¹⁾, Friedemann Wenzel¹⁾ and Mircea Radulian²⁾

***Tectonophysics* (2007), 438:33-56**

doi:10.1016/j.tecto.2007.02.016

(preprint)

(1) Geophysical Institute, University of Karlsruhe, Germany

(2) National Institute for Earth Physics, Bucharest, Romania

Contact: adrien.oth@ecgs.lu (Adrien Oth)

ABSTRACT

Several source parameters (source dimensions, slip, particle velocity, static and dynamic stress drop) are determined for the moderate-size October 27th, 2004 ($M_W=5.8$), and the large August 30th, 1986 ($M_W=7.1$) and March 4th, 1977 ($M_W=7.4$) Vrancea (Romania) intermediate-depth earthquakes. For this purpose, the empirical Green's functions method of Irikura (1983, 1986, 1999) is used to generate synthetic time series from recordings of smaller events (with $4 \leq M_W \leq 5$) in order to estimate several parameters characterizing the so-called strong motion generation area, which is defined as an extended area with homogeneous slip and rise time and, for crustal earthquakes, corresponds to an asperity of about 100 bar stress release (Miyake et al., 2003). The parameters are obtained by acceleration envelope and displacement waveform inversion for the 2004 and 1986 events and MSK intensity pattern inversion for the 1977 event using a genetic algorithm. The strong motion recordings of the analyzed Vrancea earthquakes as well as the MSK intensity pattern of the 1977 earthquake can be well reproduced using relatively small strong motion generation areas, which corresponds to small asperities with high stress drops (300 – 1200 bar) and high particle velocities (3 – 5 m/s). These results imply a very efficient high-frequency radiation, which has to be taken into account for strong ground motion prediction, and indicate that the intermediate-depth Vrancea earthquakes are inherently different from crustal events.

INTRODUCTION

The intermediate-depth earthquakes occurring in the Vrancea seismogenic zone, with a maximum instrumentally measured magnitude of 7.7, pose a significant seismic hazard to Romania and its neighboring countries Moldova and Bulgaria (e.g. Ardeleanu et al., 2005; Lungu et al., 1999; Musson, 2000; Mantysniemi et al., 2003; Sokolov et al., 2004). During the last century, four major earthquakes occurred within the Vrancea zone on November 10th 1940 ($M_W=7.7$), March 4th 1977 ($M_W=7.4$), August 30th 1986 ($M_W=7.1$) and May 30th 1990 ($M_W=6.9$). The most recent moderate shock in Vrancea occurred on October 27th 2004 ($M_W=5.8$). In the work presented here, we use the empirical Green's functions (EGF) method of Irikura (1983, 1986, 1999) to get more insight into the source parameters (source dimensions, slip, slip velocity, static and dynamic stress drop) of this earthquake and the large shocks which occurred on August 30th 1986 and March 4th 1977. Whereas the strong motion database for the latter two events is rather sparse (especially for the 1977 event, where only one single observation in Bucharest exists), the case study of the more recent event is very promising, as the number of high-quality strong motion recordings for this earthquake is by far the largest as ever recorded in Romania.

Source parameters of Vrancea earthquakes have been the subject of several previous studies (e.g. Räckers and Müller, 1982; Trifu and Oncescu, 1987; Oncescu, 1989; Gusev et al., 2002; Sokolov et al., 2005), some of these with rather different outcomes. In this study, synthetic time series (acceleration, velocity and displacement) are computed for the moderate to large Vrancea earthquakes mentioned above in a broadband frequency range (about 0.4 – 12 Hz) from smaller events using the EGF-method of Irikura (Irikura 1983, 1986, 1999) and compared with observed records. As there is only one observation available for the 1977 event, instrumentally determined intensity is compared with the observed macroseismic intensity (MSK) pattern. Minimizing the misfit between

observations and simulations enables us to find suitable models for the strong motion generation area (SMGA). A genetic algorithm is used to find acceptable solutions to this geophysical inverse problem.

Irikura's method is based on the self-similarity hypothesis, which in general assumes constant stress drop over a wide magnitude range. A detailed description of the technique is given in a separate section later in this article. Based on this scaling, this simulation approach has proven to generate data-consistent time series in a broadband frequency range using a simple source model of an extended area with homogeneous slip and rise time (e.g. Kamae and Irikura, 1998; Miyake et al., 2001, 2003). A physical interpretation for this source model has been given recently by Miyake et al. (2003), who, following the analysis of twelve crustal earthquakes in Japan, came to the conclusion that the SMGA is equivalent to an asperity within a larger rupture area, where the background slip area shows practically no stress release. The advantages of the method are that it does neither require the knowledge of the explicit shape of the slip velocity time function nor the direct estimation of path and site effects (as long as linear soil behavior is a valid approximation, which may not always be the case for very large earthquakes). On the other hand, it is not always easy to find an appropriate smaller event to be used as EGF, as it should have approximately the same location and focal mechanism and must be recorded at the same site as the target earthquake to be synthesized. As, in recent years, many Vrancea earthquakes with moment magnitude $4 \leq M_w \leq 5$ have been recorded by the K2-network described in the database section further below, the EGF-technique of Irikura is an interesting tool to investigate the strong motion generation mechanism of Vrancea earthquakes. We show that the SMGA's which explain the characteristics of strong motion recordings from intermediate-depth Vrancea events are very different from those of crustal earthquakes, indicating small asperities of high stress drops and high particle velocities.

SEISMICITY AND TECTONICS OF SE-ROMANIA

The Vrancea district, located in the South-Eastern part of the Carpathian Arc, is affected by the occurrence of frequent and strong intermediate-depth earthquakes. All these events are generated within a narrowly confined focal volume. The epicentral zone is limited to an area of about 30 x 70 km² and the seismic activity is bound to an almost vertical stripe that extends from around 80 to 200 km in depth (Trifu, 1990). Figure 1 shows a topographic map of the area, with the Vrancea source zone being located within the Carpathian arc bend.

The observed focal mechanisms of Vrancea earthquakes (e.g. Constantinescu and Enescu, 1964; Oncescu and Trifu, 1987; Trifu, 1991; Oncescu und Bonjer, 1997) as well as the results of a stress inversion by Plenefisch (1996) indicate a thrust regime with vertical extension and horizontal compression. Two types of focal mechanisms occur. The prevalent type is characterized by a NE-SW striking fault plane and perpendicular maximum compression. All events with $M_w \geq 7$ so far observed show this kind of mechanism. Fewer earthquakes have a NW-SE striking fault plane with maximum compression in the NE-SW direction.

The present tectonic setting of the region is illustrated in Figure 2. It has been interpreted by Sperner et al. (2001) as the result of a previous subduction of oceanic lithosphere with subsequent soft continental collision and slab roll back. Timing along the Carpathian arc was asynchronous and the process came to a halt 8 Ma ago. Continuous subduction along the Alpine-Carpathian system was first terminated in the Alps by continent-continent collision during the Eocene, but continued in the embayment of the European continental margin in the East between Western Europe and the Moesian platform. At this time this embayment was occupied by oceanic lithosphere. During the Mid-Miocene a gradual slab retreat forced the North-Pannonian- and the Tisia-Dacia-

block to migrate into this embayment. The migration continued until continent-continent-collisions at the edges of the embayment stopped the subduction. This happened first at the northern, then at the south-eastern and finally at the southern rim of the embayment, which forms nowadays the Vrancea region. Here the collision occurred last until about 8 Ma ago. The continent-continent-collisions formed the Carpathian mountain range and the foredeep basins filled with molasses from the mountain arc (Figure 2). The break-off of the subducted lithosphere presumably also started first in the North and continued progressively towards the South-East and South. The strong seismicity in a confined source volume beneath Vrancea is interpreted as events within a subducted slab segment not yet completely detached, in a vertical position. The general idea of a sinking lithosphere beneath the Carpathian arc was first discussed by Roman (1970). This is not only compatible with the observed thrust fault mechanisms but has been supported by regional seismic tomography (Martin et al., 2006) which images the slab and shows clear indication that the seismicity is confined to the slab.

DATABASE

All of the records from the small events (EGF-events) as well as from the October 2004 event were gathered by the accelerometer network installed by the Collaborative Research Center 461 (CRC 461) “Strong Earthquakes” of the University of Karlsruhe in cooperation with the National Institute for Earth Physics (NIEP) in Bucharest, which is operative since 1997. The network consists at present of 44 digital Kinometrics K2 instruments. Figure 1 shows only the K2-stations which provided data for this study. We can of course only make use of stations which recorded both the TARGET earthquake (large shock to be modeled) and at least one of the EGF-events associated with it.

Acceleration data from five EGF-events ($4.0 \leq M_w \leq 5.0$) were used to model the October 2004 (TARGET-A) and August 1986 (TARGET-B) earthquakes. Ideally, the

associated EGF-events should depict a similar hypocentral location as the larger shock to be modeled. Thus, our choice of EGF-earthquakes is limited to events which took place within the same depth range as the target events and the epicenters should be the closest possible to each other. Only EGF-events with $M_w \geq 4.0$ were chosen in order to ensure a reasonable signal-to-noise ratio, the latter one also being the decisive criterion for the analyzed frequency band which will be discussed below. These criteria finally limited our selected database to five EGF-earthquakes, two of them being used as EGF's for the October 2004 event and three as EGF's for the August 1986 event. The October 2004 event itself is used as EGF-event to simulate the March 1977 (TARGET-C) earthquake. The epicenter locations of the TARGET- and EGF-events together with the fault plane solutions are depicted in Figures 1 (TARGET-A and -B) and 10 (TARGET-C). The hypocentral coordinates as well as the magnitudes and origin times are listed in Table 1. The hypocentral coordinates of the events used in this study were taken from the ROMPLUS catalogue (Oncescu et al., 1999a). The fault plane solutions of the EGF-events were determined at NIEP and those of the TARGET-events were extracted from the Harvard CMT solutions catalogue.

The accelerograms from the August 1986 earthquake consist of analog recordings of an SMA-1 network operated by NIEP (Oncescu et al., 1999b), which have been scanned and digitized at NIEP. As a part of the digitization process, the records have been Ormsby filtered (for all stations utilized in this study between 0.125 – 24 Hz, except for station BMG and CFR between 0.125 – 15 Hz). As by far the largest part of the signal energy is contained in the frequency range below 12 Hz and in view of the frequency constraints imposed by the digitization, any analysis performed in this study using the digitized SMA-1 data was limited to frequencies below this limit. The digitized records have a sampling rate of 100 samples/sec.

From the March 1977 earthquake, there exists only one single analogue observation (recorded within the city of Bucharest and digitized at the Building Research Institute/Ministry of Construction, Japan). Thus it is not possible to perform a waveform inversion due to a lack of data. However, it is feasible to invert for the source parameters of TARGET-C using the MSK intensity pattern (Radu et al., 1979) and the technique of Sokolov (2002) to determine instrumental intensities.

The data acquired by the K2-network (TARGET-A and all EGF-events) have been recorded with a sampling rate of 200 samples/sec and for the purpose of this study, we reduced the sampling rate of all these data to 100 Hz (as the digitized records of the 1986 event have a sampling rate of 100 Hz).

Only the horizontal components of the S-wave were considered, as the strongest part of the S-waves is usually to be found there. The data were rotated and we finally used 15 s SH-wave signal windows that start 2 s before the S-wave onset. For the comparison between synthetics and observed data we use a frequency range restricted to 0.5 – 12 Hz for TARGET-A and 0.4 – 12 Hz for TARGET-B. Below 0.5 Hz resp. 0.4 Hz, the signal-to-noise ratio of the EGF-events recordings was not satisfactory. Above these frequencies, the signal-to-noise ratio was generally higher or equal to 2. An example for the signal-to-noise ratio analysis of the EGF-events can be found in Figure 3, where 10 s signal- and noise-windows have been used. The first and last 5 % of the time series were tapered with a cosine function and the FAS of the records were smoothed with a 0.2 Hz wide moving average filter. The signal-to-noise ratio of the K2-data is in general larger than 2 up to 20 – 25 Hz, although the largest part of the signal energy is associated with frequencies smaller than 12 Hz. Records with unclear S-wave onset or with an unacceptable signal-to-noise ratio were removed from the dataset. In total, 22 records (12 from EGF-A200209 and 10 from EGF-A200211) recorded at 14 locations were included in the inversion of

TARGET-A and 14 records (5 from EGF-B19991108, 5 from EGF-B19991114 and 4 from EGF-B200004) recorded at 6 locations were used for the inversion of TARGET-B. Concerning the inversion of TARGET-C, acceleration data from the October 2004 event (TARGET-A and EGF-C20041027) at 33 locations was used. The considered frequency range (based on a signal-to-noise ratio analysis of EGF-C200410) was 0.2 – 12 Hz.

STRESS DROP – THEORETICAL BACKGROUND

As mentioned previously, the source parameters of Vrancea earthquakes that are estimated in this study are source dimensions, slip, particle velocity and stress drop. Among these, stress drop is of very high interest since it provides not only hints on the origin of the considered events (the case of high stress drops would be compatible with an environment of subducted lithosphere, e.g. Garcia et al., 2004), but also is a key parameter in the estimation of strong ground motion. We have to distinguish between the static and dynamic stress drop in the following discussion. The dynamic stress drop $\Delta\sigma_d$ is the stress which is effectively available to drive the fault motion. Following Brune (1970), the dynamic stress drop controls the amount of high frequency energy in accelerograms, as the Fourier amplitude for frequencies beyond the corner frequency depends on the dynamic stress drop. This fact is important especially for engineering seismology purposes, as for large earthquakes, almost the complete frequency band of interest to this discipline (about 0.5 – 5 Hz) is to be found beyond the corner frequency. For instance, for a crustal earthquake of magnitude 5.5 we expect to show a corner frequency around 0.3 – 0.5 Hz. Moreover, the dynamic stress drop also controls the level of peak ground acceleration (Hanks and Johnson, 1976). However, we should note that the dynamic stress drop is in fact a proxy for the slip velocity, as was emphasized by Beresnev (2001). The static stress drop $\Delta\sigma_s$, on the other hand, is proportional to the strain change caused by the earthquake.

With \bar{D} being the average displacement on the fault and \tilde{L} the characteristic source dimension, the static stress drop can be related to the strain change $\frac{\bar{D}}{\tilde{L}}$ on the fault plane by Hooke's law:

$$\Delta\sigma_s = C_s \mu \frac{\bar{D}}{\tilde{L}}, \quad (1)$$

where C_s is a nondimensional constant whose value depends on the source geometry and the choice of \tilde{L} (Kanamori and Anderson, 1975) and μ is the shear modulus.

The dynamic stress drop is generally time-dependent and can be related to the particle slip velocity \dot{U} at one side of the fault (Brune, 1970 ; Kanamori, 1994). With the average fault displacement $\bar{D} = (2 \cdot U)$ and particle dislocation rise time τ_r , the average particle velocity at one side of the fault yields $\langle \dot{U} \rangle = \bar{D} / (2 \cdot \tau_r)$. Following Kanamori (1994), the equation given below connects $\Delta\sigma_d$ and $\langle \dot{U} \rangle$:

$$\Delta\sigma_d = C_d \frac{\mu}{v_s} \langle \dot{U} \rangle, \quad (2)$$

where C_d is a nondimensional constant of the order of 2 and v_s is the shear wave velocity. As can be seen immediately from equation (2), the average dynamic stress drop is directly proportional to the average particle velocity.

Most commonly, for crustal earthquakes, the average static stress drop is assumed to be of the same order of magnitude as the average dynamic one (Kanamori, 1994). Using several quite restrictive assumptions (e.g. circular crack, dislocation rise time of same order of magnitude than total rupture propagation time, etc.), Brune (1970, 1971) related the corner frequency of the Fourier amplitude spectrum (FAS) to the source dimensions (and thus, to the static stress drop), resulting in the well-known equation of the form:

$$f_c = C \cdot \frac{v_s}{R}. \quad (3)$$

Here, f_c is the corner frequency, v_s the shear wave velocity, R the source radius and C is a coefficient of proportionality with value $2.34/(2\pi)$. However, as Beresnev (2001) pointed out, any particular value for this coefficient is probably debatable, due to the assumptions involved in deriving the relation. Following Beresnev, the displacement on a dislocation that leads to the classical ω^2 -spectrum may be given by

$$D(t) = \bar{D} \left[1 - \left(1 + \frac{t}{\tau} \right) e^{-\frac{t}{\tau}} \right], \quad (4)$$

where \bar{D} is the final value of displacement and τ is a parameter which governs the speed of dislocation rise. The displacement and acceleration spectra are in this case:

$$\hat{U}(f) \propto \frac{M_0}{1 + \left(\frac{f}{f_c} \right)^2}, \quad (5)$$

$$\hat{A}(f) \propto (2\pi f)^2 \frac{M_0}{1 + \left(\frac{f}{f_c} \right)^2}. \quad (6)$$

\propto indicates proportionality, M_0 denotes the seismic moment and $f_c \equiv 1/(2\pi\tau)$ is the corner frequency. At frequencies larger than f_c , the acceleration spectrum is constant and proportional to $M_0 f_c^2$. Moreover, as Beresnev points out, by taking the time derivative of (4) and the definition of the corner frequency, it is easy to show that the corner frequency is proportional to the maximum slip velocity, $f_c \propto \dot{U}_{\max}$. Thus, the corner frequency and high-frequency spectral level of acceleration are directly proportional to the slip velocity, and any relationship between source dimensions (and consequently, static stress drop) and spectral parameters is subject to several major assumptions (for a detailed discussion of

these, we refer the reader to Beresnev, 2001). It should hence be noted that, although the parameter stress drop as such is well-defined, any estimation of its value is model-dependent.

Nevertheless, equation (3) is widely used in the seismological community to estimate the source dimensions of mostly moderate size earthquakes, for which the circular fault approximation is usually considered to be acceptable. This is not the case anymore for e.g. large crustal events, as the depth of the seismogenic zone limits the growth of the rupture plane in this direction, leading to a rectangular-shaped fault plane which can only grow in length when the depth of the seismogenic zone is reached. Heaton (1990) presented evidence that the particle dislocation rise time may be short for such events compared to the overall rupture time.

EMPIRICAL GREEN'S FUNCTIONS METHOD

Detailed descriptions of the empirical Green's functions method employed here can be found in Irikura (1983, 1986, 1999), Kakehi and Irikura (1996), Kamae and Irikura (1998) and Miyake et al. (2003). In the following section, the main traits of the technique are summarized. Irikura's EGF-method is based upon the self-similarity concept, which, generally speaking, assumes constant (static and average dynamic) stress drop for all magnitudes. This assumption leads to the following scaling relations (Irikura, 1999):

$$\frac{L}{l} = \frac{W}{w} = \frac{\bar{D}}{\bar{d}} = N \quad (\text{Kanamori and Anderson, 1975}) \quad (7)$$

$$\frac{\tau_R}{\tau_r} = N \quad (\text{Brune, 1970 \& 1971}), \quad (8)$$

where l , w , \bar{d} and τ_r are the source length, source width, average displacement and particle dislocation rise time of the small EGF-event and L , W , \bar{D} and τ_R are the same

parameters for the TARGET event. Thus the fault plane of the large earthquake can be constructed from N^2 equally sized subfaults, where each subfault has the size of the EGF-earthquake's fault. However, as Irikura (1999) points out, there are indications that the condition of constant stress drop does not ideally hold over wide magnitude ranges. Therefore, it is necessary to account for stress drop differences between the TARGET and EGF-events. Then equations (7) and (8) can be modified to (Irikura, 1999):

$$\frac{L}{l} = \frac{W}{w} = \frac{\tau_R}{\tau_r} = N, \quad (9)$$

$$\frac{\bar{D}}{\bar{d}} = CN. \quad (10)$$

C denotes the (static and dynamic) stress drop ratio between the large and small events.

Expressing the relations above in terms of seismic moments leads to:

$$N = \sqrt[3]{\frac{M_0}{C m_0}}, \quad (11)$$

with M_0 and m_0 being the respective seismic moments of the TARGET and the EGF-events. The simulation of the TARGET is done by summing up the contributions from the subfaults separated from each other by a time difference which depends on the location of the subelement on the fault relative to the rupture initiation point and on the rupture propagation (the rupture propagates radially away from the rupture starting point at a fixed fraction of the shear wave speed):

$$U(t) = \sum_{i=1}^N \sum_{j=1}^N \frac{r}{r_{ij}} F(t) * (C \cdot u(t)), \quad (12)$$

$$F(t) = \delta(t - t_{ij}) + \frac{1}{n'(1 - \frac{1}{e})} \sum_{k=1}^{(N-1)n'} \left[\frac{1}{e^{\frac{(k-1)}{(N-1)n'}}} \delta \left\{ t - t_{ij} - \frac{(k-1)\tau_R}{(N-1)n'} \right\} \right], \quad (13)$$

$$t_{ij} = \frac{r_{ij} - r_0}{v_S} + \frac{\xi_{ij}}{v_R}, \quad (14)$$

where $*$ denotes convolution, $U(t)$ is the synthesized waveform for the large event (acceleration, velocity or displacement) and $u(t)$ is the waveform of the small event. The terms r , r_{ij} and r_0 are the distance from the site to the hypocenter of the EGF-event, from the site to the (i,j) subfault on the rupture plane of the TARGET event and from the site to the rupture initiation subfault on the fault plane of the TARGET event, respectively. ξ_{ij} represents the distance between the rupture starting point and the (i,j) subfault, v_S and v_R are the shear wave and rupture velocities. τ_R is the rise time of the large earthquake and $F(t)$ is a filtering function which is introduced in order to prevent sags at multiples of $1/\tau_R$ in the amplitude spectra of the simulated waveforms. n' is an arbitrary integer which should be chosen much larger than N in order to shift artificial periodicities to higher frequencies than the ones of interest. Further discussions about the filtering function can be found e.g. in Miyake et al. (2003). A schematic illustration of the EGF-method as well as the shape of the filtering function is shown in Figure 4. Once the source dimensions (L and W) and the rise time (τ_R) are determined, it is possible to estimate static and dynamic stress drop, slip and slip velocity, as we will discuss in more detail later in this article.

In terms of scaling of the seismic spectra, it is assumed that both the source spectra of the TARGET and EGF-event follow the ω^{-2} spectral scaling as proposed by Brune (1970, 1971), displaying a constant spectral level equal to the seismic moment at low frequencies and a f^{-2} spectral decay at frequencies higher than the corner frequency f_C . The spectral ratios (discussed below and displayed in Figures 5 and 6) confirm this spectral scaling assumption.

ESTIMATION OF SCALING PARAMETERS

In order to get realistic simulations and reasonable inversion results, we need to obtain proper estimates for the parameters N and C . We follow Miyake et al.'s (2001, 2003) suggestion to use the spectral ratios between TARGET and EGF-events to derive these parameters for TARGET-A and TARGET-B. Assuming linear filters, the observed waveforms are a convolution of the source effect $S(t)$, propagation effect $P(t)$ and site effect $G(t)$ (lowercase letters $s(t)$, $p(t)$, $g(t)$ indicate these effects for the EGF-event). In the frequency domain, the convolution corresponds to a simple multiplication:

$$U(t) = S(t) * P(t) * G(t) \Rightarrow U(f) = S(f) \cdot P(f) \cdot G(f). \quad (15)$$

Herein, the propagation effect should be approximately identical for the main event and its empirical Green's function, i.e. $P(f)=p(f)$. Moreover, we can make the approximation $G(f)=g(f)$, which can be considered as valid only if linear soil behavior is assumed. As the peak accelerations of the records used in this study do not exceed 0.2 – 0.3 g , this approximation may be considered as reasonable. Non-linearity is commonly associated with peak accelerations larger than this threshold (e.g. Su et al., 1998).

Then, the spectral ratio should approximately correspond to the ratio of the source terms:

$$\frac{U(f)}{u(f)} \approx \frac{S(f)}{s(f)} \quad (16)$$

If the FAS are assumed to show the ω^{-2} shape (Brune, 1970, 1971), the source terms can be written as:

$$S(f) = \frac{M_0}{1 + \left(\frac{f}{f_C}\right)^2}, \quad (17)$$

where f_C is the corner frequency. With equation (17), the ratio between the spectra of the large and small event is ($f_{C,T}$ and $f_{C,E}$ being the respective corner frequencies):

$$\frac{S(f)}{s(f)} = \frac{M_0}{m_0} \cdot \frac{1 + \frac{f^2}{f_{C,E}^2}}{1 + \frac{f^2}{f_{C,T}^2}}. \quad (18)$$

Thus, in the low frequency limit, the spectral ratio tends to a constant level M_0/m_0 , whereas in the high frequency limit it tends to a constant level of value $(M_0/m_0)(f_{C,T}/f_{C,E})^2$. With equation (11) it can be easily seen that

$$\frac{M_0}{m_0} = CN^3, \quad (19)$$

$$\frac{M_0}{m_0} \cdot \left(\frac{f_{C,T}}{f_{C,E}} \right)^2 = CN. \quad (20)$$

By fitting a theoretical spectral ratio following equation (18) to the log average of the observed spectral ratios, we can estimate the parameters C and N . At each station, the FAS of the TARGET record and the corresponding EGF-record and their spectral ratio were computed. The log frequency axis was divided into 20 bins within the frequency range 0.5 – 20 Hz (in this frequency range, the signal-to-noise ratio of the small events generally exceeded a factor of 2) for TARGET-A and 0.4 – 12 Hz for TARGET-B event. As the magnitudes of the EGF-events used to simulate TARGET-B are somewhat higher than those used to simulate TARGET-A, the analyzed frequency range is large enough to constrain the high-frequency plateau of the spectral ratio with enough accuracy.

For each bin, the log average of the frequency points within this bin was computed for each spectral ratio function and assigned to the bins' central frequency. Finally, the log average and standard deviations for all the spectral ratios within each frequency bin were obtained. A theoretical spectral ratio of the form given by equation (18) was fitted to the observations by searching the minimum of the weighted (each frequency bin was weighted according to its standard deviation) least squares.

The results of this procedure are listed in Table 2 and graphically displayed in Figure 5 for TARGET-A and in Figure 6 for TARGET-B. Note the unusually high corner frequency as well for TARGET-A (around 1.6 Hz, practically identically determined with both EGF-events) as for its EGF-events. The analysis of TARGET-B raises a few problematic aspects which have to be discussed. First of all, the database for this event is rather sparse compared to the one for TARGET-A. Second, a general problem of this methodology if (very) large earthquakes are considered, is the fact that the corner frequency is to be found close to or, as in our case, below the lowest frequency analyzed (which is 0.4 Hz in this case, due to signal-to-noise ratio constraints for the small event). Thus, the low-frequency plateau (meaning the moment ratio) is rather difficult, if not impossible to firmly constrain with this methodology in the case of large earthquakes.

Nevertheless, the obtained results may be regarded to be plausible, as the corner frequency for TARGET-B (about 0.25 – 0.30 Hz) is in good agreement with the value determined in an earlier study by Oncescu (1989) and the moment ratio (respectively the low-frequency spectral level) between TARGET-B and the EGF-events is close to the value that would be expected if the seismic moments would be deduced from the moment magnitudes (using the moment magnitude scale given by Hanks and Kanamori, 1979) extracted from the ROMPLUS catalogue (Oncescu et al., 1999a). Yet, these difficulties have to be kept in mind, especially in view of the interpretation of the inversion results following in the later sections.

If we would try to anticipate at this point the results of the following inversion by looking at the spectral ratios presented above, we would expect to find quite small SMGA's and short particle dislocation rise times (which would be equivalent to high slip velocities and stress drops), as the corner frequencies are generally very high.

INVERSION PROCEDURE

Synthetic acceleration, velocity and displacement time series were computed using the EGF-methodology described in the preceding sections. Besides the parameters N and C which have been determined earlier, we need to specify the following five parameters characterizing the SMGA (Miyake et al., 2003): length, width, rise time and the coordinates of the rupture initiation point along strike and dip.

Parameter Optimization Using Genetic Algorithms

In order to estimate these parameters, we used a genetic algorithm to minimize the residuals between observed and synthetic displacement waveforms (low frequencies) and acceleration envelopes (high frequencies) for TARGET-A and -B and between instrumental and observed MSK intensity for TARGET-C. Genetic algorithms (e.g. Goldberg, 1989, Haupt and Haupt, 1998) are guided search methods that evaluate successive generations of trial models, where the first generation consists of randomly chosen models. They do neither require linearization nor a single adequate starting model and allow to invert for suitable models even in the case of a highly non-linear inverse problem with a large number of controlling parameters. As a rule, the parameters give rise to trade-offs which may result in highly complex misfit surfaces in the multi-dimensional parameter space. Genetic algorithms have been used to solve a variety of geophysical inverse problems (e.g. Sambridge and Drijkoningen, 1992; Lomax and Snieder, 1994; Miyake et al., 2003; Scherbaum et al., 2006).

After the creation of a random initial population and evaluation of the misfit of its members, genetic algorithms work in three steps based on evolutionary principles:

1. natural selection (the fittest members of the population survive, or, respectively, those with highest misfit die off)

2. mating and crossover (the survivors mate in pairs and produce offspring by recombination of their genes)
3. mutation (random changes are included in the genes of some of the offspring)

A plethora of variants, some of which are very complex, exist for these genetic operators, especially for crossover and mutation operations.

As such, geophysical inverse problems may have several (or even numerous) distinct acceptable solutions rather than a unique one. In the case of complex misfit surfaces, the genetic algorithm method has proven to be a powerful optimization tool as it contains a convergent component by combining the features of the best (meaning lowest misfit) models in each generation but is still able to escape local minima of the misfit function through random mutation or (lucky) crossover. There are many ways of implementing the different steps of a genetic algorithm (e.g. Haupt and Haupt, 1998). Often, genetic algorithms are configured to find an ‘optimum’ solution by rapid convergence and tend to end up in a local minimum rather than finding the global one. This is the well-known problem of premature convergence. Hence, it is important to carefully balance the convergent and random features of the algorithm and to perform several runs with different initial populations in order to get an idea of the acceptable solution space. However, there is no guarantee that a genetic algorithm will really find the global minimum, especially if several solutions with comparable misfit exist. The challenge is in that case to determine all of these different solutions rather than only one of them.

One unsatisfactory feature of genetic algorithms in general is the fact that they have to be tuned in view of the problem to be solved. This tuning includes a certain degree of quite subjective and problem-dependent decisions for which a general rule is difficult to provide (population size, search range, crossover and mutation rates, mating and crossover scheme, etc.). Nonetheless, genetic algorithms are very powerful especially in

the case of large parameter spaces and complicated misfit surfaces, where purely random search or direct inversion methods often fail.

Description of the Algorithm Used in this Study

Because the inversion problem would be poorly constrained if all the parameters necessary for the EGF simulations were treated as free parameters, we restricted the inversion to the five ones mentioned above: length L , width W , rise time τ_R , rupture starting point along strike and dip (normalized to the interval [0,1] when inverting using two (TARGET-A) or three (TARGET-B) EGF-events simultaneously with different scaling factors N – the distance along strike and dip has been normalized and for each trial simulation with one of these EGF-events, the rupture initiation subfault which corresponds most closely to the normalized position has been determined). N and C have been determined using the spectral ratios, and the shear wave and rupture velocities have been set to $v_S = 4.5$ km/s and $v_R = \zeta v_S$. We performed the inversion for ζ equal to 0.9, 0.8 and 0.7, which are commonly assumed values. The algorithm was run five times for each considered rupture velocity.

The chromosomes (or trial models) are composed of a binary representation of trial values for the five parameters characterizing the SMGA. The crossover and mutation rates were set to $P_c = 0.6$ and $P_m = 0.04$ respectively. We started the algorithm with an initial population of 150 chromosomes. The fittest 100 of these were chosen to run the rest of the 200 iterations. Of these 100 trial models, the 2 best were kept unchanged from generation to generation and the 2 with largest misfit died off. The remaining 98 chromosomes were allowed to mate following a rank weighted ‘roulette wheel’. Crossover of the chromosomes was performed using a two-point scheme.

The algorithm described above has a good balance in terms of convergent and stochastic tendencies. The somewhat larger first generation ensures a sufficient initial

sampling of the parameter space and the convergence of the algorithm is not overly fast, as it contains only a very weak form of elitism (only the best 2% of the chromosomes are kept to go unchanged into the next generation), the crossover rate is not very high and the rank weighting ensures that members of the population with much lower misfit than average are not excessively weighted, which can be the case using cost (or misfit) weighting and lead to premature convergence into the local minimum defined by an extraordinary fit chromosome. All models with a misfit below some threshold which arise during each run are stored in a separate array in order to examine the diversity of the acceptable solutions found.

Inversion for TARGET-A and TARGET-B Using Waveform Data

Velocity and displacement time series were obtained by integration and bandpass-filtering within the frequency range 0.5 – 12 Hz for TARGET-A and its empirical Green's functions respectively 0.4 – 12 Hz for TARGET-B. As a measure of misfit, we used the residuals of the displacement waveforms u and acceleration envelopes e (similarly defined e.g. in Suzuki and Iwata, 2005 ; Suzuki et al., 2006):

$$misfit = \sum_{records} \left(\frac{\sum_t (u_{obs} - u_{syn})^2}{\sqrt{\sum_t u_{obs}^2 \sum_t u_{syn}^2}} + \frac{\sum_t (e_{obs} - e_{syn})^2}{\sqrt{\sum_t e_{obs}^2 \sum_t e_{syn}^2}} \right) \quad (21)$$

As mentioned in the database section, the records were 15 s long, starting 2 s prior to the S-wave onset, which has been picked on the velocity traces.

Inversion for TARGET-C Using the MSK Intensity Pattern

A problematic issue which arises for the large 1977 Vrancea earthquake (TARGET-C) is that there is only one strong motion observation (located at INCERC, National Institute for Building Research, in the city of Bucharest) available. Due to this simple fact, a waveform inversion in order to retrieve the SMGA parameters is not possible. Even pure

trial and error modeling in order to explain this observation would be highly speculative, as we speak about a non-linear problem dependent on 7 controlling parameters (N , C , L , W , τ_R , rupture starting point along strike and dip). However, there is a large amount of data available for the October 2004 (TARGET-A and EGF-C200410), which can be used as an EGF-event for TARGET-C, as both focal mechanisms and locations are very close to each other. As a macroseismic intensity map (Radu et al., 1979) exists for the March 1977 earthquake, we decided to evaluate instrumental intensity and to perform an inversion using the observed intensity pattern.

In principle, the inversion procedure is identical to the one described in the preceding section, with the main difference being the misfit criterion:

$$misfit = \sum_{records} (|Intensity_{observed} - Intensity_{simulated}|). \quad (22)$$

15 s long SH-wave records (frequency range 0.2 – 12 Hz) for TARGET-C were simulated at 33 locations and their instrumental intensities determined following Sokolov (2002), whose technique makes use of the full FAS of the S-phase to compute intensity (MMI or MSK scale) estimates. In few words, intensity is derived from the FAS by comparison with empirical reference spectra for each intensity level determined from a dataset of about 1150 worldwide recordings. This comparison is done using a probabilistic approach. Thus, the intensity-based inversion performed here can be viewed as a sort of frequency-domain (although indirect, of course, and without any phase information) inversion. These values were compared to the observed MSK intensities using equation (22) and the genetic algorithm described above was used to explore the solution space. Due to the lack of waveform data, it is of course not possible to seriously evaluate (with one usable record) the parameters C and N by spectral ratio analysis as done for TARGET-A and TARGET-B. Thus, C was set to be 1 (which, generally in terms of self-similarity when no evaluation is possible and, specifically in view of the stress drop ratios

determined for other Vrancea events in Table 2 ranging between 0.7 – 2, is considered to be a reasonable choice) and N was computed to be 6 using the ratio of the seismic moments calculated from the moment magnitudes with the relation of Hanks and Kanamori (1979).

As the inversion for TARGET-C is not based on waveform data, we introduced a further constraint concerning the aspect ratio of the SMGA which is reasonable in view of the results obtained for TARGET-A and -B. We performed two different inversions for TARGET-C: a) we enforced that the SMGA should be square and b) the aspect ratio was set to be the same as the one which resulted for TARGET-A.

The macroseismic maps of the two large Vrancea earthquakes of 1977 (Radu et al., 1979) and 1986 (Radu et al., 1987) presented in this article are displayed in Figure 7 and based on the MSK seismic intensity scale. As the original macroseismic information was not available anymore, the intensities and isoseismals were digitized, a work which was performed at the Institute of Remote Sensing and Photogrammetry of the University of Karlsruhe.

The observed record at station INCERC (named INB in this study) as well as the prior inversion for the SMGA of TARGET-A were used as an independent additional information, as we compared the simulation at station INB using the source model inverted from the intensity distribution with the latter observation. The inverted source model should of course hopefully not completely contradict this record. Additionally, the subfault size resulting from the inversion should be in quite close agreement with the SMGA size of TARGET-A. As we will discuss below, both these requirements are indeed fulfilled by the inverted solution.

RESULTS AND DISCUSSION

The search ranges for the parameters were set to 0.5 – 15 km for L and W and 0.01 – 2 s for τ_R during the inversion for the source parameters for TARGET-A ($M_W = 5.8$), 1 – 40 km for L and W and 0.05 – 5 s for τ_R during the inversion of TARGET-B ($M_W = 7.1$) and 2.5 – 60 km for L (W was computed from the enforced aspect ratio) and 0.05 – 5 s for τ_R during the inversion of TARGET-C ($M_W = 7.4$). All subfaults were searched for the rupture starting point location. For TARGET-A and -B, we performed a combined inversion with all respective EGF-events. The inversion results with lowest misfit values are summarized in Tables 3, 4 and 5. For TARGET-A, the lowest misfit values were obtained using a rupture velocity $v_R = 0.9 v_S$, while the best results for TARGET-B were computed with $v_R = 0.7 v_S$ or $v_R = 0.8 v_S$. As observed data for TARGET-A were used as input (EGF-C200410) for the inversion of TARGET-C, the latter one was only performed for the rupture velocity $v_R = 0.9 v_S$ in view of the results obtained during the earlier inversion of TARGET-A.

Waveforms and Intensity Pattern

Some waveform examples simulated with the lowest misfit models and, for comparison, the respective observations are shown in Figure 8 (TARGET-A) and Figure 9 (TARGET-B). For each station, the acceleration time series are shown on the left and the displacement time series on the right. For almost all waveforms, the fit ranges from fair to good, although in few cases the amplitudes are slightly misestimated (with a maximum factor of about 2). The outcome of the macroseismic intensity inversion for TARGET-C's SMGA is displayed in Figure 10. The observed isoseismals are shown as black lines (compare with intensity map in Figure 7). Although the scatter is rather large, the main features of the intensity pattern can be explained acceptably well with our inverted solution. If only the inverted intensity values would be known, one would probably draw

a continuous isoseismal line for intensity VIII around the epicentral area and Bucharest instead of separate patches, and this intensity VIII area would be a bit larger than the observed ones. The small patch of large intensity (VIII) around Craiova cannot be reproduced with our data. However, as only one observation in that area has been included into our inversion and intensity values reported at a given location are strongly dependent on local site conditions, it is not possible to draw any conclusion about this fact which would be representative. The station included in the inversion may simply have been located at a site where the ground shaking was not that strong. In conclusion, taking into consideration all the problems and uncertainties related with the compilation of such intensity maps and the unavoidable standard deviation on the empirical relations between FAS and intensity, we regard the overall results as acceptable.

Analysis of the Uniqueness of the Inversion Results

In general, the algorithm converges to similar best solutions during all of the consecutive runs with different initial trial models. However, this is clearly not the case for TARGET-B using a rupture velocity of $v_R = 0.9 v_S$. Here it is evident to see that there are at least two preferred ‘best’ solutions. This ambiguity for TARGET-B may simply be due to the fact that a) the waveform database available for this inversion was sparser than the one for TARGET-A and b) it was more difficult to estimate the parameters C and N from the spectral ratios, as mentioned above.

From the fact that generally higher misfits and these ambiguities arise only for a certain value of the ratio rupture- to shear wave velocity, we can also come to the conclusion that this v_R/v_S -ratio is less likely than the ones showing the lowest values of misfit. However, as the differences in misfit are not excessively large, we must note at this point that we can argue that these higher misfit solutions may be less probable, but they cannot be strictly ruled out.

We may expect for a non-linear inversion problem several distinct (and almost equivalent in terms of misfit) solutions. In the case of e.g. two solutions with very similar misfits, it strongly depends a) on the initial set of trial models, b) on the configuration of the genetic algorithm and c) on the ‘luck’ in the genetic operations whether the algorithm will finally make its way into one or the other minimum. The goal that we want to achieve, however, is to find both solutions. Table 6 gives an overview on the variability of the solution space. There, the mean values of each parameter as well as their standard deviations for the 2500 fittest models (500 fittest found in each run) are summarized. From this table and the corresponding minimum-misfit models (Tables 3, 4 and 5), it is obvious that the SMGA parameters are well constrained for both TARGET-A and TARGET-C. TARGET-B shows well constrained parameters for both $v_R = 0.7 v_S$ and $v_R = 0.8 v_S$, but a strong variability in width, rise time and rupture initiation point along dip for the case $v_R = 0.9 v_S$. However, these large standard deviations are due to the fact that the algorithm finally converges either to a width around 30 km and a rise time of about 0.4 s (e.g. run 1 in Table 4) or to a width of about 4 km and a rise time around 0.25 s (e.g. run 2 in Table 4) with different rupture initiation points along dip. Both of these solution types can be found during each run in the list of the fittest models. Thus we may rather talk about two different low-misfit solutions than strong variability and the inversion procedure nevertheless enables us to clearly restrict the solution space. The mean misfit for $v_R = 0.9 v_S$ is about 10 – 15 % larger than the one for the other considered rupture velocities, a fact which indicates that the former solutions are less probable. In the next few paragraphs we will thus restrict our discussion to the lowest misfit models presented in Tables 3, 4 and 5.

Dimensions and Rise Time of the SMGA's for Vrancea Earthquakes

The dimensions as well as the rise time of these SMGA models for TARGET-A (around 2 km²) and TARGET-C (around 65 km² for a square SMGA and 90 km² using the same aspect ratio as the lowest misfit model for TARGET-A) are remarkably small, a fact which is consistent with the large corner frequency of TARGET-A. For TARGET-B, the lowest misfit model (around 160 km²) does not depict such a small SMGA, even though we have to keep in mind that there is a solution (with different rupture velocity) with only 5% higher misfit and much smaller SMGA (around 25 km²). The corresponding rise time is also quite small for all models. An encouraging fact from the inversion of TARGET-C is that a) the only observed record is quite well fitted by the simulation using our intensity-derived SMGA model (Figure 11) and b) the subfault size and rise time determined is very close to the SMGA size and rise time for the lowest misfit model of TARGET-A (resp. EGF-C200410), as well for a square SMGA as for one with aspect ratio 1:1.5.

First, this is a good indication that it was not a completely false estimate to use the stress drop ratio $C = 1$ between these two events. Secondly, it should be emphasized at this point that the waveform inversion for the SMGA parameters of TARGET-A and the intensity pattern inversion performed for TARGET-C both provide information on TARGET-A's SMGA which is essentially independent of each other and leads to very similar SMGA sizes and rise times for the October 2004 earthquake (once as the main shock, once as the subevent). Thus, these results are indeed consistent with each other. Radulian et al. (2007) determined similar dimensions for this event's asperity from the pulse width of the source time function after deconvolution of an empirical Green's function.

Physical Interpretation and Discussion

As was mentioned earlier, several studies concerning the source parameters of Vrancea earthquakes exist and especially their stress drop values are a matter of an ongoing debate. Different approaches have been used to determine stress drop values. The assumption that the area where aftershocks occur is identical to the rupture area was used by Räckers and Müller (1982) and Trifu and Oncescu (1987) to estimate the static stress drops of the 1977 and 1986 major Vrancea earthquakes and led to stress drop values around 50 bar. Another common approach is to determine the corner frequency and seismic moment from the displacement spectra and to compute an estimate for the static stress drop from these data using Brune's (1970, 1971) source model. Gusev et al. (2002) found static stress drops of the order of 100 to 200 bar for the two large earthquakes of March 1977 and August 1986 using long-range (several hundred to thousands km) and teleseismic data. Oncescu (1989) applied this method on analog strong motion recordings of the 1986 large earthquake and determined a Brune stress drop estimate for this event of approximately 850 bar. Furthermore, the latter study contains three estimates of the dynamic stress drop of the 1986 earthquake, which range between 950 bar and 1.4 kbar. If long-range or even teleseismic data are used, these methods estimate an average stress drop value over the whole rupture plane rather than asperity stress drop. Thus, it is not surprising that Räckers and Müller (1982), Trifu and Oncescu (1987) and Gusev et al. (2002) reach rather low stress drop estimates. In order to get insight into the asperity stress release, which is the most relevant concerning strong motion prediction, it is indispensable to analyze local strong motion data, as we do in this article. Oncescu's (1989) high asperity stress drop value for the 1986 earthquake was also derived from such data.

Interpreting our results in terms of stress drop and other physical source parameters is not a trivial task either, since the estimates of these parameters are heavily dependent on whether the SMGA is considered to be an asperity within a larger background rupture area that shows no significant stress drop, but, due to its slipping, contributes to the seismic moment of the event, or a simple crack releasing the complete seismic moment. However, a simple crack model would lead to exorbitantly high stress release estimates, which would violate any physical rationale and be inconsistent with earlier studies on aftershock distributions and on the occurrence of Vrancea earthquakes as a result of a distribution of local stress heterogeneities at depth (Trifu and Radulian, 1989, 1991).

Miyake et al. (2003) interpreted the SMGA to be equivalent to an asperity in the stress-free field based on a dataset of crustal earthquakes where low-frequency slip inversions were available. Such slip inversions do unfortunately not exist for intermediate-depth Vrancea earthquakes. In order to estimate the spatial extent of the total rupture plane, the only source of information that we can rely on is the aftershock distribution. The dimensions of the total rupture area are needed in order to estimate which part of the seismic moment is released by the SMGA compared to the background slip area. In view of the unavoidable uncertainties both in the determination of the total rupture dimensions and the SMGA parameters, it has to be noted that the stress drop, slip and slip velocity estimates derived below are naturally only approximate.

For TARGET-B (August 30th 1986), Oncescu (1989) proposed an asperity of about 160 km² within a total rupture area of about 700 km², the latter one having been estimated by the occurrence of aftershocks. The size of our lowest misfit SMGA is surprisingly close to this asperity size estimate. For TARGET-A (October 27th 2004), the situation is complicated by the fact that very few aftershocks occurred (Bonjer, pers. comm., 2006), which makes it impossible to estimate the extent of the rupture using this information. For

TARGET-C (March 4th 1977), Hartzell (1979) and Råkers and Müller (1982) proposed fault plane dimensions ranging around 2000 km² (Hartzell proposed a circular fault with 25 km radius, Råkers and Müller favored a spatial extent of about 60 x 40 km).

If we follow the interpretation of Miyake et al. (2003), the SMGA is considered to be an asperity within a larger background slip area which is assumed to have no stress drop. Based on the work of Madariaga (1979) and Boatwright (1988), they proposed to estimate the stress drop of the SMGA with the following equation, assuming a single asperity model:

$$\Delta\sigma_{SMGA} = \frac{7}{16} \cdot \frac{M_0}{Rr^2}, \quad (23)$$

where M_0 is seismic moment of the earthquake, R is the radius of the equivalent circular total rupture plane and r is the radius of the equivalent circular SMGA. Formula (23) simply means nothing else than computing the stress drop for a circular crack of radius r with a seismic moment reduced by the factor r/R to account for the moment release due to the background slip. We can then (with this reduced seismic moment) use the definition $M_0 = \mu \cdot A \cdot \bar{D}$, with A being the fault (or asperity) area and \bar{D} its average displacement, and the rise time τ_R to compute estimates for the slip and slip velocity within the SMGA.

With the SMGA- and total rupture area estimates discussed above, the approximate values listed in Table 7 have been computed (assuming $\mu = 7 \cdot 10^{10} \text{ N/m}^2$). The stress drop for the October 2004 event has been deduced from the one of the March 1977 event (remember that we set their stress drops to be equal which must be viewed, of course, as an approximation). From this stress drop estimate and the SMGA size, a total fault plane area of approximately 30 – 40 km² can be deduced for the October 2004 earthquake.

Two major interesting conclusions arise from these results. First, the March 1977 as well as the October 2004 earthquakes seem to show 2 – 3 times larger (static) stress drops

than the August 1986 event. The second striking feature is the fact that all the three moderate to large events analyzed seem to be similar from the dynamic point of view, as they depict almost identical particle velocities and thus (see equation (2)), almost identical dynamic stress drops ranging around 1kbar. These large particle velocities are responsible for the strong high-frequency radiation.

As a lower bound of the seismic energy radiated by the SMGA can be given by $E_S = (\Delta\sigma_{SMGA} / 2) \cdot A \cdot \bar{D}$ (e.g. Kanamori, 1994), a formula which is based on the assumptions that the frictional stress σ_f is constant and the final stress after the earthquake on the fault is equal to σ_f , the March 1977 SMGA could have released about 3 times more energy than the one of the August 1986 earthquake. However, as there is a larger difference between the dynamic stress drop (≈ 1 kbar) and static stress drop (≈ 300 bar), it may also be possible to explain the SMGA of the 1986 earthquake by an abrupt-locking model (Kanamori, 1994) with a sudden drop in friction e.g. at the time slippage begins (for the constant friction model to hold, the average static and dynamic stress drop should have the same order of magnitude). In that case, the seismic energy release computed using the simplified formula above would underestimate the radiated energy. Thus, the question of energy release is not answerable without speculation.

The differences in stress drop between the 1977/2004 and 1986 earthquakes (and, which we should not forget, their subevents used as EGF's) lead us to the possible conclusion that the events taking place in the depth range 90 – 110 km are somewhat different in their physical source properties and their energy budget from the deeper events (130 – 150 km). Yet, due to the fact that only three moderate to large instrumentally recorded earthquakes (which we have discussed in this article) still represent a quite scarce strong motion database (even though it is the largest available database for Vrancea earthquakes), the evidence presented in this article is not yet

sufficient to firmly constrain or generalize such a hypothesis. Moreover, the earlier discussed ambiguity for TARGET-B should not be forgotten at this point, as we also have inverted a smaller SMGA solution (e.g. solution 3 for 90% v_s , Table 4), even though clearly less probable in terms of misfit.

A final interesting issue is the strong damage produced in Bucharest city during the 1977 earthquake, whereas the city was not that heavily harmed during the 1986 event. The SMGA's with lowest misfits for the three analyzed earthquakes are displayed as sketches in Figure 12. The 'grid' composed of the subevents is only displayed for the 1977 earthquake, as the other events have been inverted using several different EGF's. Therefore, the normalized position derived during the inversions has been used to plot the approximate location of rupture initiation. As can be seen, the directivity effect towards Bucharest within the SMGA is larger for the 1977 earthquake than for 1986, but it may be questioned whether this effect alone and the somewhat higher magnitude in 1977 is enough to explain the quite large differences in macroseismic intensities (Figure 7). Our results indicate that the 1977 earthquake most probably depicted a much larger stress release than the 1986 event and that the differences in intensities may mostly be due to this fact. As the SMGA size for the October 2004 earthquake is exceptionally small, directivity effects are probably less relevant for this event.

CONCLUSIONS

The empirical Green's functions method of Irikura was used to gain more insights into the source processes of intermediate-depth Vrancea earthquakes. In this study, the largest number of high quality strong motion data ever available for a source study of Vrancea earthquakes has been used to determine source models for the moderate size October 27th 2004 ($M_w = 5.8$) and the two large March 4th 1977 ($M_w = 7.4$) and August 30th 1986 ($M_w = 7.1$) events. The application of Irikura's method to Vrancea earthquakes leads to small

strong motion generation areas. According to the definition of Miyake et al. (2003), these areas (inside of which constant slip and slip velocity is supposed) are interpreted as asperities within a total background fault plane with practically no stress drop. Therefore, for a given seismic moment, a smaller strong motion generation area and rise time is equivalent to higher stress drops and particle velocities. Our results show stress drop and particle velocity values within these asperities ranging between 300 and 1200 bar and 3 and 5 m/s respectively. Crustal earthquakes usually show stress drop values between 10 and 100 bar and particle velocities lower than 1 – 2 m/s (e.g. Kanamori, 1994). Miyake et al. (2003) presented evidence that the strong motion generation areas of crustal earthquakes show a stress release of about 100 bar. Thus, the events treated here are inherently different. The large particle velocities imply a particularly efficient high-frequency radiation, which is easily visible by simply looking at the records. These facts are of high importance for strong ground motion prediction for large earthquakes in the area. In addition, we could speculate, on the basis of the results presented in this paper, that there is a change in earthquake source properties with depth in the Vrancea seismogenic zone. Note however that the existent database does not yet allow for more than speculation on this matter.

ACKNOWLEDGMENTS

This study was carried out in the Collaborative Research Center (CRC) 461 ‘Strong Earthquakes: a Challenge for Geosciences and Civil Engineering’, which is funded by the Deutsche Forschungsgemeinschaft (German Research Foundation) and supported by the state of Baden-Württemberg and the University of Karlsruhe. We thank K. Irikura and H. Miyake for providing their simulation program and their advice on its use. B. Sperner’s comments on the tectonics of SE-Romania are highly appreciated. V. Sokolov kindly made his instrumental intensity code available to us and gave helpful comments on the

earliest version of the manuscript. K.-P. Bonjer helped with the intensity maps and valuable discussions. W. Weisbrich (Institute of Remote Sensing and Photogrammetry of the University of Karlsruhe) digitized and geo-referenced the intensity values. Some figures were drawn with GMT (Wessel and Smith, 1995). The authors are grateful for the constructive comments of two anonymous reviewers which helped to improve the article significantly.

REFERENCES

- Ardeleanu, L., G. Leydecker, K.-P. Bonjer, H. Busche, D. Kaiser and T. Schmitt (2005). Probabilistic seismic hazard map for Romania as a basis for a new building code. *Nat. Haz. Earth Sys. Sc.*, 5, 679-684.
- Beresnev, I.A. (2001). What we can and cannot learn about earthquake sources from the spectra of seismic waves. *Bull. Seism. Soc. Am.*, 91, 397-400.
- Boatwright, J. (1988). The seismic radiation from composite models of faulting. *Bull. Seism. Soc. Am.*, 78, 489-508.
- Brune, J.N. (1970). Tectonic stress and the spectra of seismic shear waves from earthquakes. *J. Geophys. Res.*, 75, 4997-5009.
- Brune, J.N. (1971). Correction. *J. Geophys. Res.*, 76, 5002.
- Constantinescu, L. and D. Enescu (1964). Fault-plane solutions for some Romanian earthquakes and their seismotectonic implication. *J. Geophys. Res.*, 69, 667-674.
- Garcia, D., S.K. Singh, M. Herraiz, J.F. Pacheco and M. Ordaz (2004). Inslab earthquakes of Central Mexico: Q, source spectra, and stress drop. *Bull. Seism. Soc. Am.*, 94, 789-902.
- Goldberg, D.E. (1989). Genetic Algorithms in Search, Optimization and Machine Learning. Addison-Wesley, New York.
- Gusev, A., M. Radulian, M. Rizescu and G. F. Panza. Source scaling of intermediate-depth Vrancea earthquakes (2002). *Geophys. J. Int.*, 151, 879-889.
- Hanks, T. C. and D. A. Johnson (1976). Geophysical assessment of peak accelerations. *Bull. Seism. Soc. Am.*, 66, 959-968.

- Hanks, T. C. and H. Kanamori (1979). A moment magnitude scale, *J. Geophys. Res.*, 84, 2348-2350.
- Hartzell, S. (1979). Analysis of the Bucharest strong ground motion record for the March 4, 1977 Romanian earthquake. *Bull. Seism. Soc. Am.*, 69, 513-530.
- Haupt, R.L. and S.E. Haupt (1998). Practical Genetic Algorithms. A Wiley-Interscience publication, John Wiley & Sons, New York, 1998.
- Heaton, T. (1990). Evidence for and implications of self-healing pulses of slip in earthquake rupture. *Phys. Earth Planet. Inter.*, 64, 1-20.
- Irikura, K. (1983). Semi-Empirical Estimation of Strong Ground Motions during Large Earthquakes. *Bull. Dis. Prev. Res. Inst., Kyoto Univ.*, 33, Part 2, No. 298, 63-104.
- Irikura, K. (1986). Prediction of strong acceleration motions using empirical Green's function, in *Proceedings of the 7th Japan earthquake engineering symposium*, 151-156.
- Irikura, K. (1999). Techniques for the simulation of strong ground motion and deterministic seismic hazard analysis, in *Proceedings of the advanced study course seismotectonic and microzonation techniques in earthquake engineering: integrated training in earthquake risk reduction practices*, Kefallinia, 453-554.
- Takehi, Y. and K. Irikura (1996). Estimation of high-frequency wave radiation areas on the fault plane by the envelope inversion of acceleration seismograms. *Geophys. J. Int.*, 125, 892-900.
- Kamae, K. and K. Irikura (1998). Source Model of the 1995 Hyogo-ken Nanbu Earthquake and Simulation of Near-Source Ground Motion. *Bull. Seismol. Soc. Am.*, 88, 400-412.
- Kanamori, H. (1994). Mechanics of earthquakes. *Ann. Rev. Earth Planet. Sci.*, 22, 207-237.
- Kanamori, H. and D. L. Anderson (1975). Theoretical basis of some empirical relations in seismology. *Bull. Seism. Soc. Am.*, 65, 1073-1095.
- Lomax, A. and R. Snieder (1994). Finding sets of acceptable solutions with a genetic algorithm with application to surface wave group dispersion in Europe. *Geophys. Res. Lett.*, 21, 2617-2620.
- Lungu, D., T. Cornea and C. Nedelcu (1999). Hazard assessment and site-dependent response for Vrancea earthquakes, in *Vrancea earthquakes: tectonics, hazard and*

- risk mitigation*, F. Wenzel, D. Lungu and O. Novak, Editors, Kluwer Academic Publishers, Dordrecht, Netherlands, 251-268.
- Madariaga, R. (1979). On the relation between seismic moment and stress drop in the presence of stress and strength heterogeneity. *J. Geophys. Res.*, 84, 2243-2250.
- Mantysniemi, P., V. I. Marza, A. Kijko and P. Retief (2003). A new probabilistic seismic hazard analysis for the Vrancea (Romania) seismogenic zone, *Natural Hazards*, 29, 371-385.
- Martin, M., F. Wenzel and the CALIXTO working group (2006). High-resolution teleseismic body wave tomography beneath SE-Romania (II): Imaging of a slab detachment scenario, *Geophys. J. Int*, 164, 579-595.
- Miyake, H., T. Iwata and K. Irikura (2001). Estimation of rupture propagation direction and strong motion generation area from azimuth and distance dependence of source amplitude spectra. *Geophys. Res. Lett.*, 28, 2727-2730.
- Miyake, H., T. Iwata and K. Irikura (2003). Source characterization for broadband ground-motion simulation: Kinematic heterogeneous source model and strong motion generation area. *Bull. Seism. Soc. Am.*, 93, 2531-2545.
- Musson, R. M. W. (2000). Generalised seismic hazard maps for the Pannonian basin using probabilistic methods, in *Seismic Hazard of the Circum-Pannonian Region*, G. F. Panza, M. Radulian and C.-I. Trifu, Editors, Birkhäuser Verlag, Basel, Switzerland, 147-169.
- Oncescu, M. C. (1989). Investigation of a high stress drop earthquake on August 30, 1986 in the Vrancea region. *Tectonophysics*, 163, 35-43.
- Oncescu, M. C. and K.-P. Bonjer (1997). A note on the depth recurrence and strain release of large Vrancea earthquakes. *Tectonophysics*, 272, 291-302.
- Oncescu, M. C. and C. I. Trifu (1987). Depth variation of moment tensor principal axes in Vrancea (Romania) seismic region. *Annales Geophysicae*, 5B, 149-154.
- Oncescu, M. C., V. I. Marza, M. Rizescu and M. Popa (1999a). The Romanian earthquake catalogue between 984-1997, in *Vrancea earthquakes: tectonics, hazard and risk mitigation*, F. Wenzel, D. Lungu and O. Novak, Editors, Kluwer Academic Publishers, Dordrecht, Netherlands, 43-48.
- Oncescu, M. C., K.-P. Bonjer and M. Rizescu (1999b). Weak and strong ground motion of intermediate depth earthquakes from the Vrancea region, in *Vrancea earthquakes: tectonics, hazard and risk mitigation*, F. Wenzel, D. Lungu and O. Novak, Editors, Kluwer Academic Publishers, Dordrecht, Netherlands, 27-42.

- Plenefisch, T. (1996). Untersuchungen des Spannungsfeldes im Bereich des Rheingrabens mittels der Inversion von Herdflächenlösungen und Abschätzung der bruchspezifischen Reibungsparameter. *Ph. D. Dissertation*, Universität Karlsruhe (TH), Germany, 128 pp.
- Radu, C., G. Polonic and I. Apopei (1979). Macroseismic field of the March 4, 1977 Vrancea earthquake. *Tectonophysics*, 53, 185-186.
- Radu, C., A. Utale and V. Winter (1987). The August 30, 1986 Vrancea earthquake. Seismic intensity distribution. *National Institute for Earth Physics Report, II, A-3*.
- Radulian, M., K-P Bonjer, E. Popescu, M. Popa, C. Ionescu and B. Grecu (2007). The October 27th, 2004 Vrancea (Romania) earthquake. *ORFEUS newsletter*, 7, no. 1.
- Räkers, E. and G. Müller (1982). The Romanian earthquake of March 4, 1977: III. Improved focal model and moment determination. *J. Geophys.*, 50, 143-150.
- Roman, C (1970). Seismicity in Romania – Evidence for the Sinking Lithosphere. *Nature*, 228, 1176-1178.
- Sambridge, M. and G. Drijkoningen (1992). Genetic algorithms in seismic waveform inversion. *Geophys. J. Int.*, 109, 323-342.
- Scherbaum, F., F. Cotton and H. Staedtke (2006). The estimation of minimum-misfit stochastic models from empirical ground-motion prediction equations. *Bull. Seis. Soc. Am.*, 96, 427-445.
- Sokolov, V. Yu. (2002). Seismic intensity and Fourier acceleration spectra: Revised relationships. *Earthquake Spectra*, 18, 161-187.
- Sokolov, V. Yu., K.-P. Bonjer and F. Wenzel (2004). Accounting for site effects in probabilistic assessment of seismic hazard for Romania and Bucharest: a case of deep seismicity in Vrancea zone. *Soil Dynamics and Earthquake Engineering*, 24, 929-947.
- Sokolov, V., K.-P. Bonjer, M. Oncescu and M. Rizescu (2005). Hard rock spectral models for intermediate depth Vrancea, Romania, earthquakes. *Bull. Seism. Soc. Am.*, 95, 1749-1765.
- Sperner, B., F. P. Lorenz, K.-P. Bonjer, S. Hettel, B. Müller and F. Wenzel (2001). Slab break-off - abrupt cut or gradual detachment? New insights from the Vrancea region (SE Carpathians, Romania). *Terra Nova*, 13, 172-179.

- Su, F., J. G. Anderson and Y. Zeng (1998). Study of weak and strong ground motion including nonlinearity from the Northridge, California, earthquake sequence. *Bull. Seism. Soc. Am.*, 88, 1411-1425.
- Suzuki, W. and T. Iwata (2005). Source characteristics of interplate earthquakes in northeast Japan inferred from the analysis of broadband strong-motion records. *Eos Trans. AGU*, 86 (52), Fall Meet. Suppl., Abstract S43A-1040.
- Suzuki, W. and T. Iwata (2006). Source model of the 2005 west off Fukuoka prefecture earthquake estimated from the empirical Green's function simulation of broadband strong motions. *Earth Planets Space*, 58, 99-104.
- Trifu, C.-I. (1990). Detailed configuration of intermediate seismicity in Vrancea region. *Revista de Geofisica*, 46, 33-40.
- Trifu, C.-I. (1991). The study of Vrancea earthquake mechanisms by a composite technique. *Rev. Roum. Phys.*, 36, 457-469.
- Trifu, C.-I. and M. C. Oncescu (1987). Fault geometry of August 30, 1986 Vrancea earthquake. *Annales Geophysicae*, 5B, 727-730.
- Trifu, C.-I. and M. Radulian (1989). Asperity distribution and percolation as fundamentals of earthquake cycle. *Phys. Earth Planet. Int.*, 58, 277-288.
- Trifu, C.-I. and M. Radulian (1991). Frequency-magnitude distribution of earthquakes in Vrancea: Relevance for a discrete model. *J. Geophys. Res.*, 96, 4301-4311.
- Wessel, P. and W.H.F. Smith (1995). New version of the Generic Mapping Tool released. *Eos*, 76, 329.

Figure 1. Topographic map of the Carpathian area. The Vrancea seismic zone is located where the Carpathian arc is bending from NW-SE toward W. The epicenters of the earthquakes utilized in this study are depicted by stars (large stars: October 27th 2004 and August 30th 1986 TARGET-A resp. B events) and the corresponding focal mechanisms are shown. The focal mechanisms of the EGF-events are lined up in columns with respect to their associated main shock. The information for the March 4th 1977 event is depicted in Figure 10. The K2-accelerometers which provided data from at least one EGF- and the corresponding TARGET event are marked by inverse triangles and their three letter station code.

Figure 2. Sketch of the present tectonic settings and geology of the Carpathian region. It is assumed that the subducting slab is at the last stage of its break-off beneath the Vrancea region (star), while it is completely detached along the rest of the Carpathian arc.

Figure 3. Example for the evaluation of the signal-to-noise ratio. The signal shown is the transverse component at station BER from EGF-A200211 (see Table 1). Upper part: acceleration time series, where the respective signal and noise windows are indicated. Lower part: Fourier amplitude spectra of signal and noise windows.

Figure 4. Illustration of the EGF-method of Irikura (modified after Miyake et al., 2003). Part a) schematically shows the faults of the target and the EGF-events, part b) illustrates the shape of the filtering function.

Figure 5. Spectral ratios of TARGET-A to EGF-A200209 (upper row) and to EGF-A200211 (lower row). In the left column the average values with the standard deviations and the best fitting theoretical function are shown for each case. In the right column the spectral ratios for all sites are displayed. For an explanation of the event identifiers, see Table 1.

Figure 6. Spectral ratios of TARGET-B to EGF-B19991108 (upper row), EGF-B19991114 (middle row) and EGF-B200004 (bottom row). Same plots as explained in Figure 5.

Figure 7. Observed macroseismic intensity maps (MSK scale) of the March 4th 1977 (top) and August 30th 1986 (bottom) earthquakes, compiled by Bonjer (pers. comm., 2006). The stars indicate the epicenter of the respective earthquakes. Explanations are included in the text.

Figure 8. Example of the outcome for the TARGET-A inversion (several simulated traces using EGF-A200211 shown here) at six locations. For each station, the observed (top) and simulated (bottom) acceleration (left) and displacement (right) 15 s SH-waveforms for the lowest misfit model are displayed. Each set of corresponding observed and simulated traces are scaled to the same maximum value.

Figure 9. Example of the outcome for the TARGET-B inversion (simulated traces using EGF-B19991108 shown here) at five locations (same plot as Figure 8).

Figure 10. Comparison of simulated and observed intensities for the March 4th 1977 earthquake. The black lines indicate the observed isoseismals, whereas the colored dots show the simulated intensity values at each station for the lowest misfit model. The simulated intensities are additionally displayed close to each dot. The locations (stars) and focal mechanisms of TARGET-C and EGF-C200410 are included in the map.

Figure 11. Upper part: Comparison of acceleration (left) and displacement (right) observed and simulated SH-waveforms at station INB (which are almost identical to the EW-component) of the March 1977 (TARGET-C) earthquake. Lower part: Comparison of Fourier amplitude spectra.

Figure 12. Sketches of the SMGA lowest misfit models for the three moderate to large Vrancea earthquakes considered in this study. The relative dimensions are scaled correctly. The (approximate) rupture initiation locations are depicted by a star. The March 1977 (square) SMGA is shown with its subevents (as the inversion was performed using one EGF only). Note the very similar size of the SMGA of the October 2004 and the subevent of the March 1977 earthquakes.

Table 1. Hypocentral coordinates, moment magnitudes and origin times of the events used in this study. The smaller earthquakes used to generate the synthetics are characterized by the identification code EGF whereas the respective main shock is referenced to as TARGET. The information shown in this table was gathered from the ROMPLUS-catalogue (Oncescu et al., 1999a).

Event ID	Date	Origin Time	Latitude [°]	Longitude [°]	Depth [km]	M _w
EGF-A200209	2002/09/06	05:04:02	45.64	26.43	105	4.1
EGF-A200211	2002/11/03	20:30:23	45.74	26.86	90	4.0
EGF-B19991108	1999/11/08	19:22:52	45.55	26.35	138	4.6
EGF-B19991114	1999/11/14	09:05:59	45.52	26.27	132	4.6
EGF-B200004	2000/04/06	00:10:39	45.75	26.64	143	5.0
EGF-C200410	2004/10/27	20:34:36	45.78	26.73	99	5.8
TARGET-A	2004/10/27	20:34:36	45.78	26.73	99	5.8
TARGET-B	1986/08/30	21:28:37	45.52	26.49	132	7.1
TARGET-C	1977/03/04	19:21:54	45.77	26.76	94	7.4

Table 2. Parameters M_0/m_0 , $f_{C,T}$, $f_{C,E}$, N and C obtained from the spectral ratio analysis.

The exact procedure is described in the text.

Event ID	$\frac{M_0}{m_0}$	$f_{C,T}$ [Hz]	$f_{C,E}$ [Hz]	N	C	Number of stations
TARGET-A/EGF-A200209	211	1.7	8.3	5	1.7	12
TARGET-A/EGF-A200211	651	1.6	10.8	7	1.9	10
TARGET-B/EGF-B19991108	8144	0.3	4.0	16	2.0	5
TARGET-B/EGF-B19991114	7134	0.3	4.9	17	1.5	5
TARGET-B/EGF-B200004	914	0.3	3.1	11	0.7	4

Table 3. Lowest misfit models for 5 consecutive runs of the genetic algorithm for TARGET-A ($M_w= 5.8$), inverted using both EGF-A-events. The algorithm was run for 3 different ratios of rupture velocity to shear wave velocity ($v_R= 0.7 \cdot v_S$, $v_R= 0.8 \cdot v_S$, $v_R= 0.9 \cdot v_S$). The position of rupture initiation along strike and dip is given as a normalized value between 0 and 1.

	Run	L [km]	W [km]	τ_R [s]	pos. along strike	pos. along dip	Misfit
$v_R= 0.7 \cdot v_S$	1	0.73	1.08	0.06	0.3	0.5	54.24
	2	0.73	1.08	0.06	0.3	0.4	54.24
	3	0.67	0.73	0.19	0.3	0.6	54.87
	4	0.62	1.08	0.07	0.3	0.4	54.33
	5	0.82	1.36	0.12	0.3	0.6	54.99
$v_R= 0.8 \cdot v_S$	1	0.81	1.23	0.15	0.3	0.6	54.14
	2	0.96	1.27	0.13	0.3	0.6	54.09
	3	0.95	1.29	0.13	0.3	0.6	54.09
	4	0.96	1.27	0.14	0.3	0.6	54.13
	5	0.95	1.35	0.14	0.3	0.7	54.20
$v_R= 0.9 \cdot v_S$	1	0.95	1.43	0.15	0.3	0.7	53.72
	2	1.16	1.78	0.11	0.3	0.7	53.62
	3	1.16	1.78	0.11	0.3	0.7	53.62
	4	1.04	1.39	0.13	0.3	0.6	53.75
	5	0.96	1.33	0.15	0.3	0.7	53.68

Table 4. Lowest misfit models for 5 consecutive runs of the genetic algorithm for TARGET-B ($M_W=7.1$), inverted using all three EGF-B-events. The algorithm was run for 3 different ratios of rupture velocity to shear wave velocity ($v_R=0.7\cdot v_S$, $v_R=0.8\cdot v_S$, $v_R=0.9\cdot v_S$). The position of rupture initiation along strike and dip is given as a normalized value between 0 and 1.

	Run	L [km]	W [km]	τ_R [s]	pos. along strike	pos. along dip	Misfit
$v_R=0.7\cdot v_S$	1	10.12	13.10	0.36	0.2	1.0	30.06
	2	12.98	12.62	0.26	0.4	1.0	28.75
	3	12.84	12.60	0.26	0.4	1.0	28.74
	4	10.54	13.13	0.26	0.2	1.0	29.07
	5	10.75	13.26	0.26	0.2	1.0	28.96
$v_R=0.8\cdot v_S$	1	14.31	18.14	0.36	0.3	1.0	29.16
	2	14.87	18.88	0.28	0.3	1.0	28.77
	3	14.69	20.96	0.31	0.3	1.0	29.14
	4	14.34	18.45	0.36	0.3	1.0	29.00
	5	15.02	18.86	0.28	0.3	1.0	28.92
$v_R=0.9\cdot v_S$	1	6.15	33.74	0.41	0.4	0.7	32.33
	2	5.86	3.98	0.27	0.4	0.2	30.42
	3	6.58	3.70	0.25	0.4	0.1	30.14
	4	5.87	27.43	0.43	0.4	0.9	32.20
	5	5.24	34.61	0.42	0.4	0.7	31.77

Table 5. Lowest misfit models for 5 consecutive runs of the genetic algorithm for TARGET-C ($M_W=7.4$), inverted using EGF-C200410. The algorithm was run for a 90% ratio of rupture velocity to shear wave velocity ($v_R=0.9\cdot v_S$). The SMGA was once supposed to be square, once to have an aspect ratio 1:1.5 ($L:W$). The position of the rupture initiation subfault is not expressed as a normalized value in the interval [0,1], but absolutely (the number in parentheses is the scaling factor $N=6$).

<i>Square SMGA</i>	Run	L [km]	W [km]	τ_R [s]	pos. along strike	pos. along dip	Misfit
$v_R=0.9\cdot v_S$	1	8.07	8.07	0.97	1 (6)	4 (6)	25.45
	2	8.10	8.10	0.97	1 (6)	4 (6)	25.45
	3	8.13	8.13	0.96	1 (6)	4 (6)	25.45
	4	8.12	8.12	0.96	1 (6)	4 (6)	25.45
	5	8.11	8.11	0.96	1 (6)	4 (6)	25.45
<i>Aspect ratio 1:1.5</i>	Run	L [km]	W [km]	τ_R [s]	pos. along strike	pos. along dip	Misfit
$v_R=0.9\cdot v_S$	1	7.88	12.05	0.74	1 (6)	3 (6)	26.35
	2	7.89	12.07	0.74	1 (6)	3 (6)	26.35
	3	7.79	11.91	0.73	1 (6)	3 (6)	26.40
	4	7.60	11.63	0.73	1 (6)	3 (6)	26.35
	5	7.60	11.63	0.73	1 (6)	3 (6)	26.35

Table 6. Mean and standard deviations of SMGA parameters of the 2500 best models found in 5 consecutive runs (the 500 best models found in each run) of the genetic algorithm for all TARGET events. For TARGET-A and TARGET-B, the position of the rupture initiation point is given as a normalized value in the interval [0,1], whereas it is given absolutely for TARGET-C.

TARGET-A	L [km]	W [km]	τ_R [s]	pos. along strike	pos. along dip
$v_R = 0.7 \cdot v_S$	0.73 ± 0.13	1.00 ± 0.22	0.11 ± 0.06	0.32 ± 0.07	0.52 ± 0.13
$v_R = 0.8 \cdot v_S$	0.86 ± 0.16	1.13 ± 0.25	0.16 ± 0.03	0.32 ± 0.05	0.65 ± 0.08
$v_R = 0.9 \cdot v_S$	1.08 ± 0.21	1.40 ± 0.26	0.14 ± 0.04	0.32 ± 0.03	0.67 ± 0.09
TARGET-B	L [km]	W [km]	τ_R [s]	pos. along strike	pos. along dip
$v_R = 0.7 \cdot v_S$	11.03 ± 1.42	13.00 ± 1.21	0.30 ± 0.06	0.28 ± 0.10	0.95 ± 0.07
$v_R = 0.8 \cdot v_S$	14.65 ± 0.80	19.75 ± 1.40	0.34 ± 0.06	0.30 ± 0.04	0.93 ± 0.06
$v_R = 0.9 \cdot v_S$	5.52 ± 0.96	15.03 ± 13.57	0.56 ± 0.42	0.37 ± 0.04	0.51 ± 0.32
TARGET-C (<i>aspect ratio 1:1.5</i>)	L [km]	W [km]	τ_R [s]	pos. along strike	pos. along dip
$v_R = 0.9 \cdot v_S$	8.17 ± 2.95	12.18 ± 4.42	0.90 ± 0.49	1.02 ± 0.15	2.92 ± 0.39
TARGET-C (<i>square</i>)	L [km] / W [km]		τ_R [s]	pos. along strike	pos. along dip
$v_R = 0.9 \cdot v_S$	8.19 ± 2.29		1.45 ± 0.86	1.05 ± 0.22	4.07 ± 0.46

Table 7. Approximate static stress drop, particle velocity and slip estimates for the lowest misfit SMGA models. For TARGET-C, the upper row contains the estimates for an SMGA with aspect ratio 1:1.5, whereas the lower row depicts the estimates for the square SMGA.

Event ID	$\Delta\sigma_{SMGA}$ [bar]	$\langle\dot{U}\rangle$ [m/s]	\bar{D} [m]
TARGET-A (October 2004)	900 – 1200	3.5 – 4.5	0.8 – 1.0
TARGET-B (August 1986)	300	4.0	2.2
TARGET-C (March 1977)	900	3.5	5.0
	1200	3.0	5.5

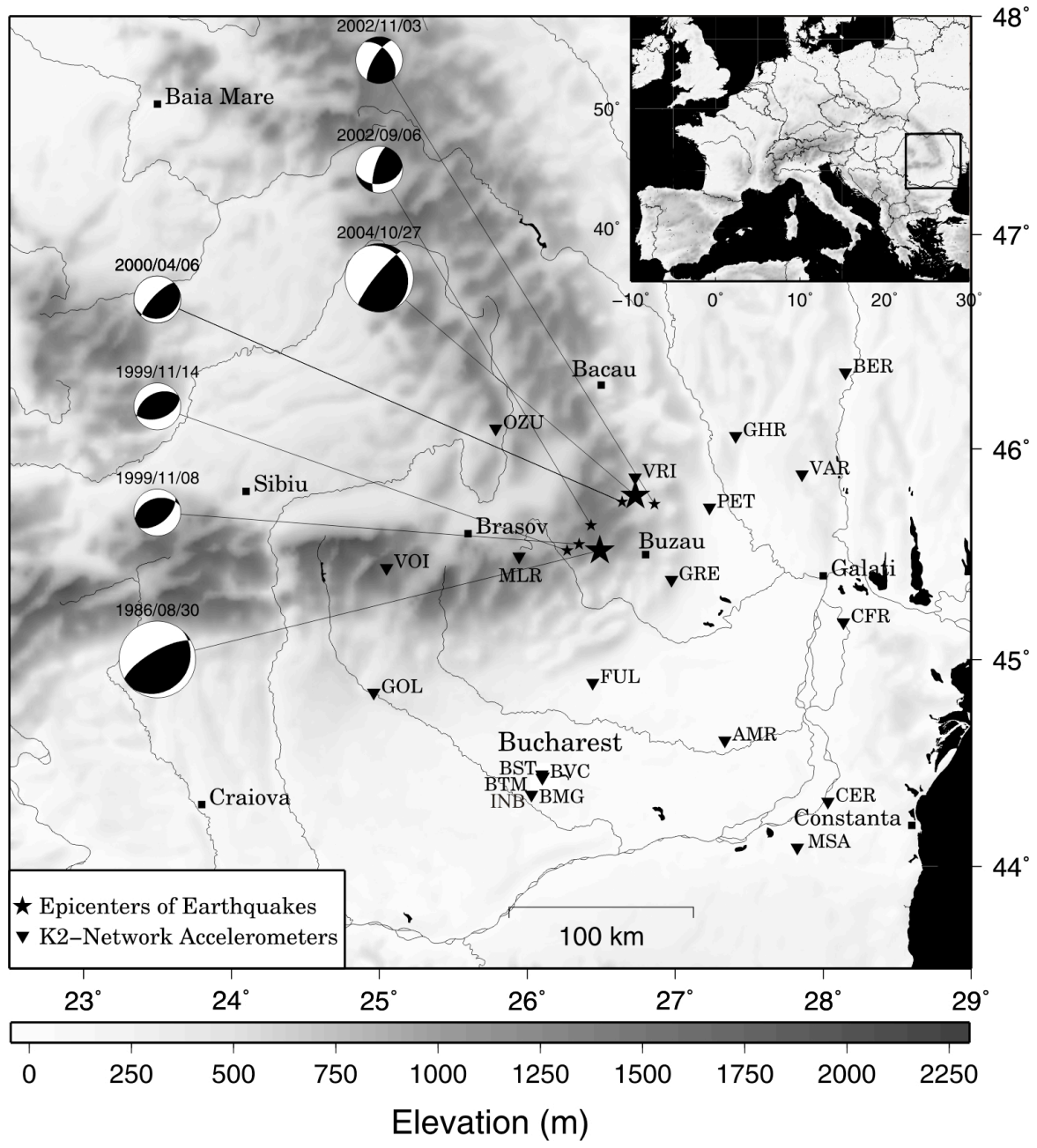
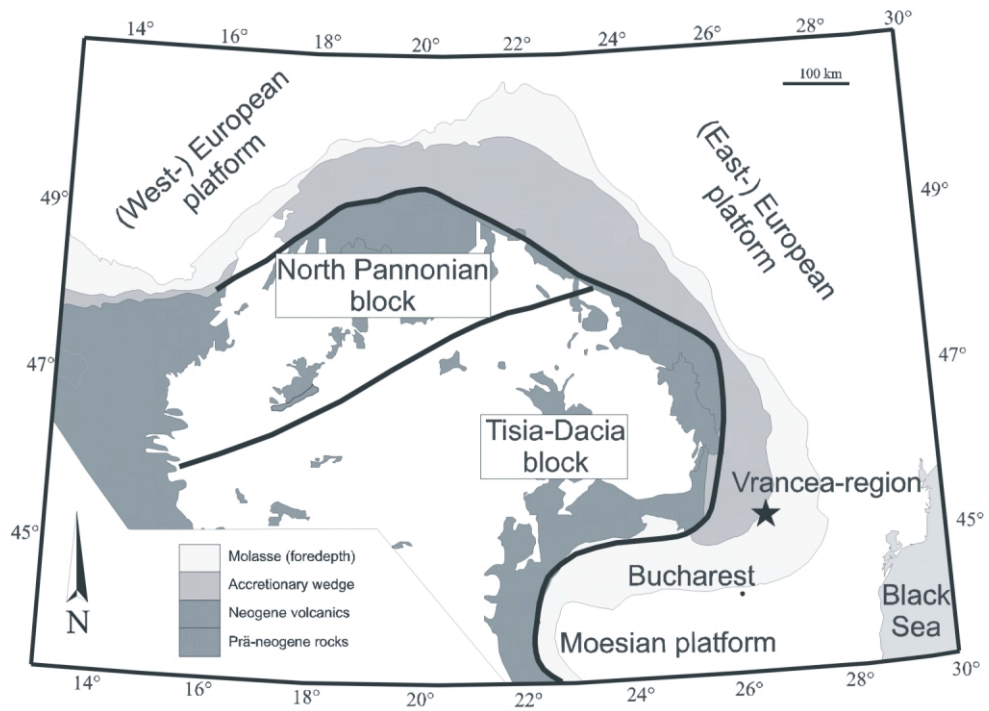


Figure 1



Modified after Sperner et al. (2001)

Figure 2

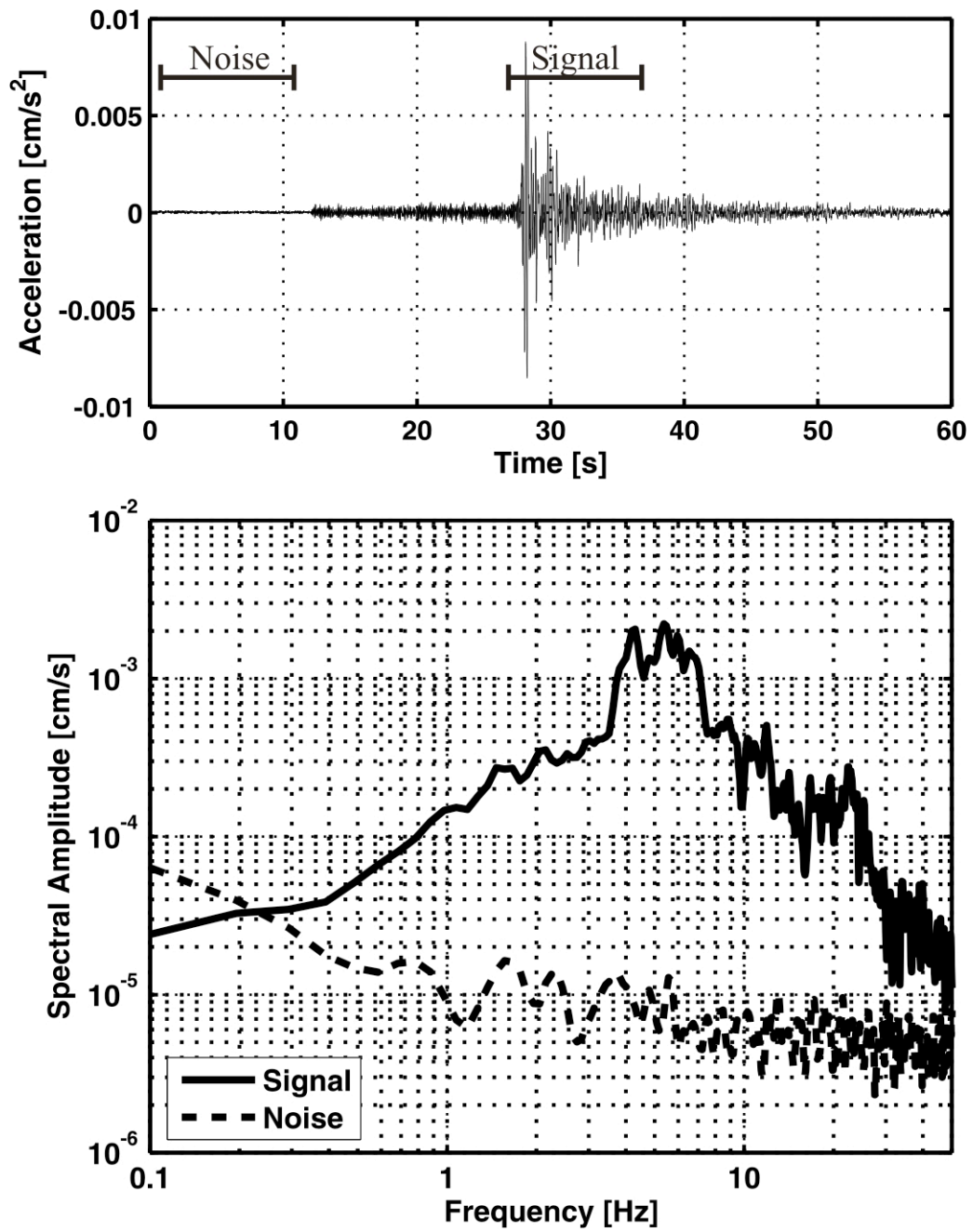


Figure 3

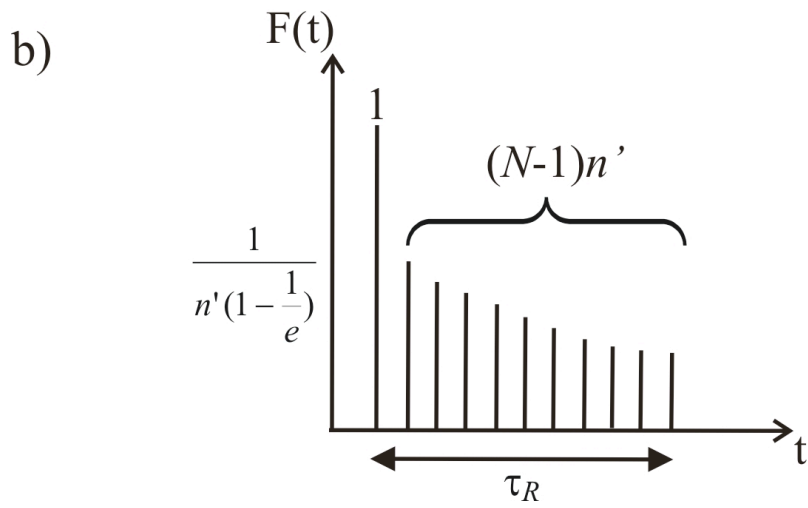
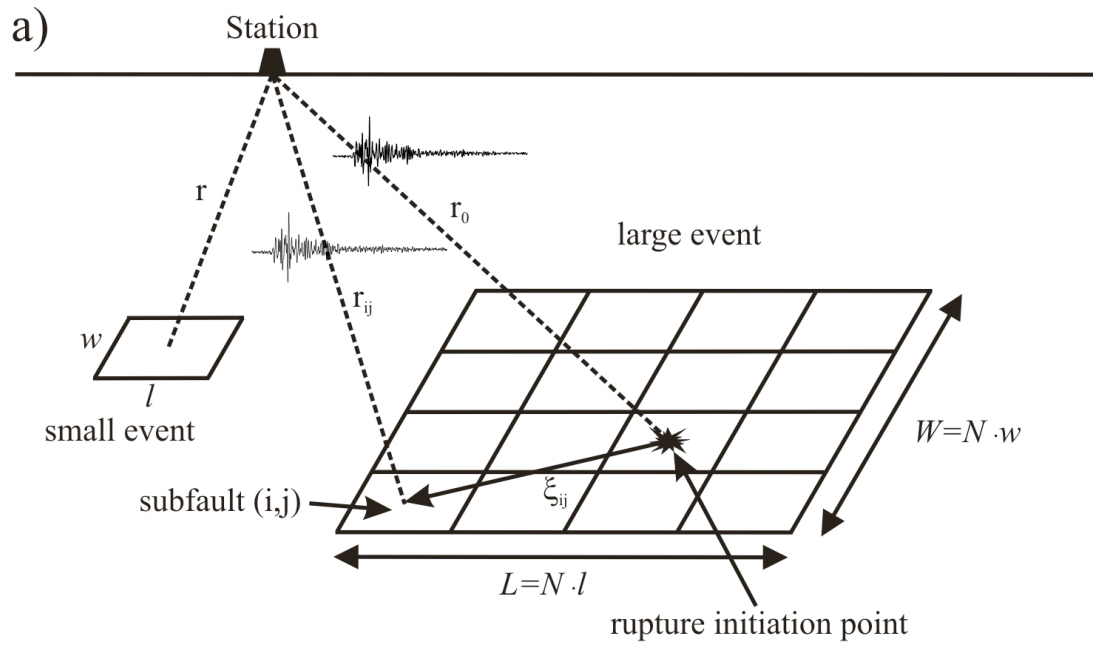


Figure 4

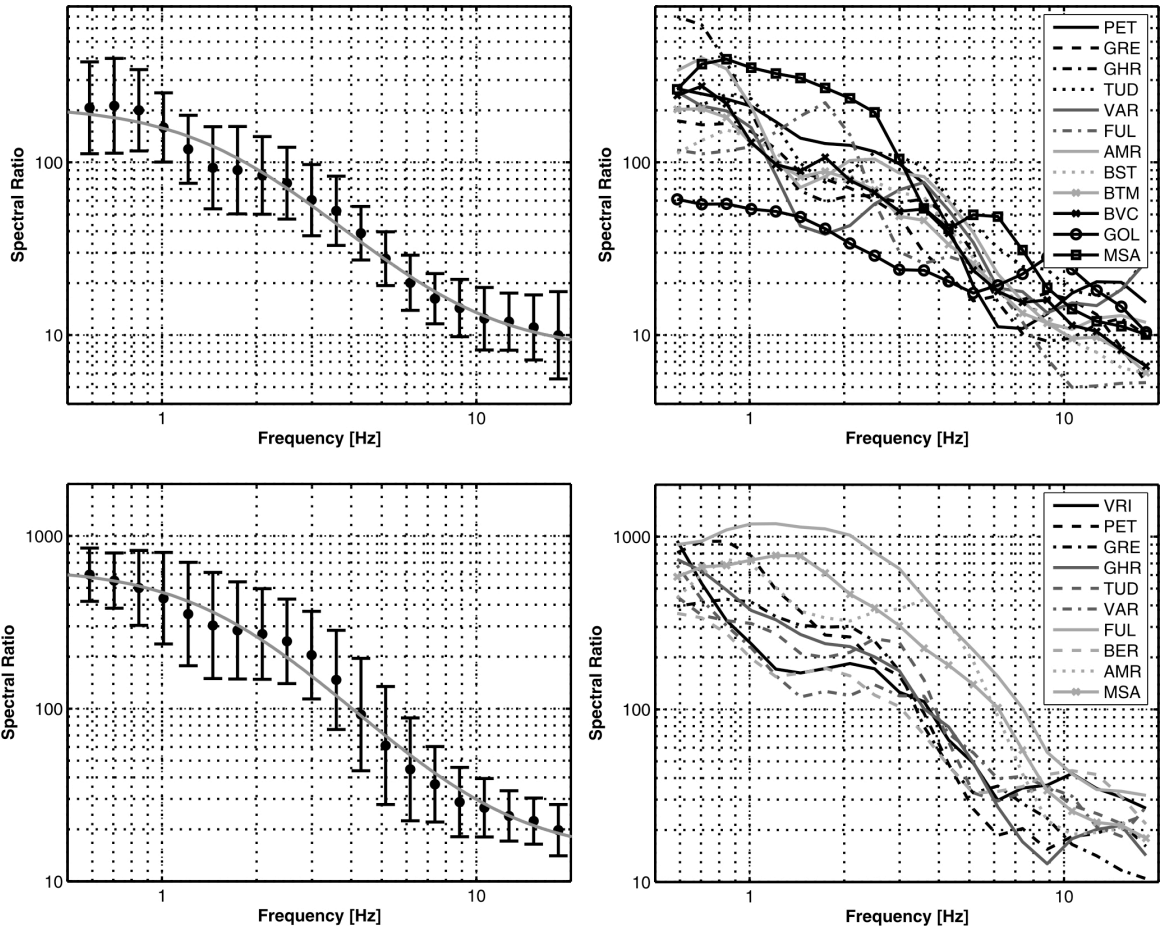


Figure 5

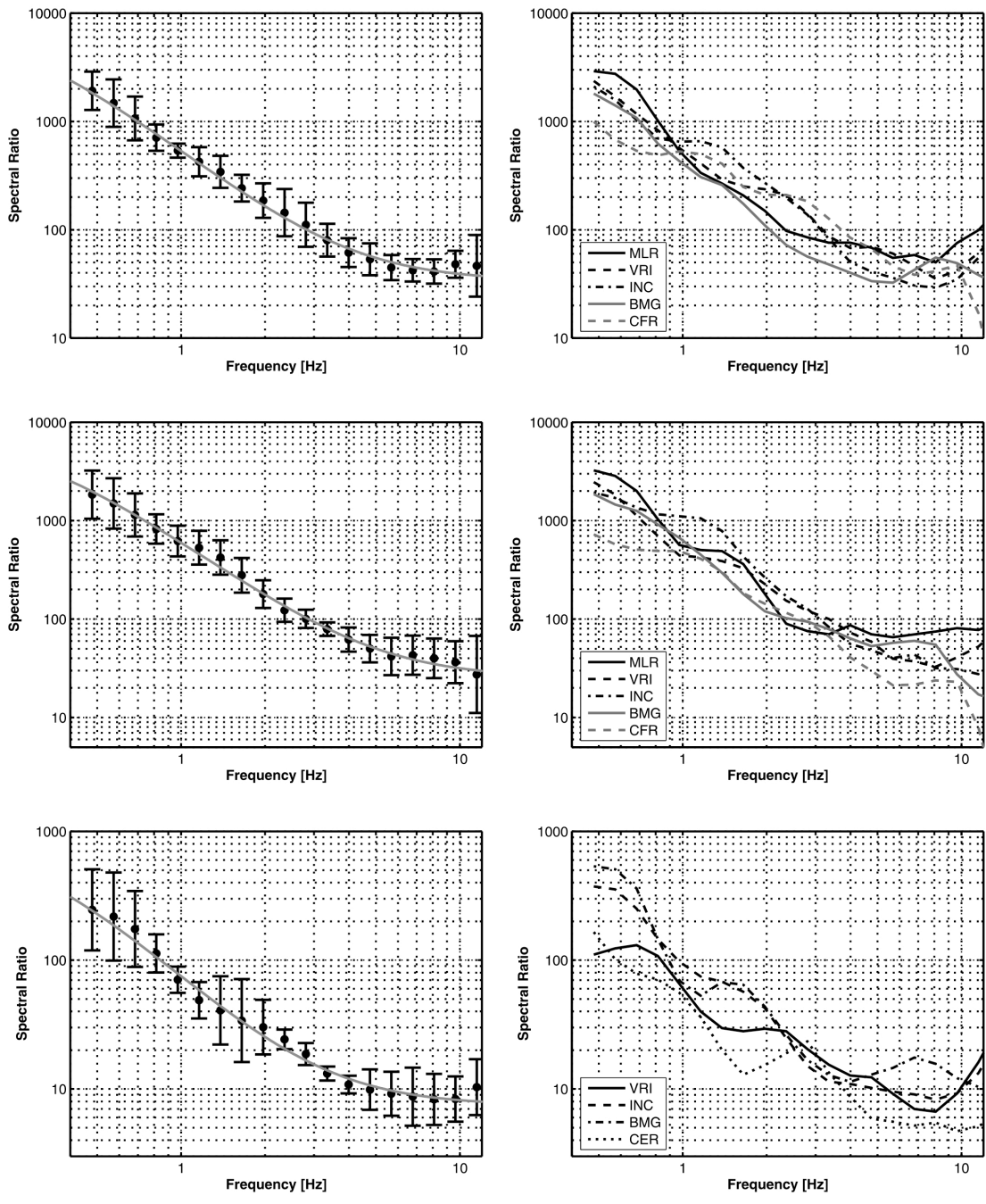


Figure 6

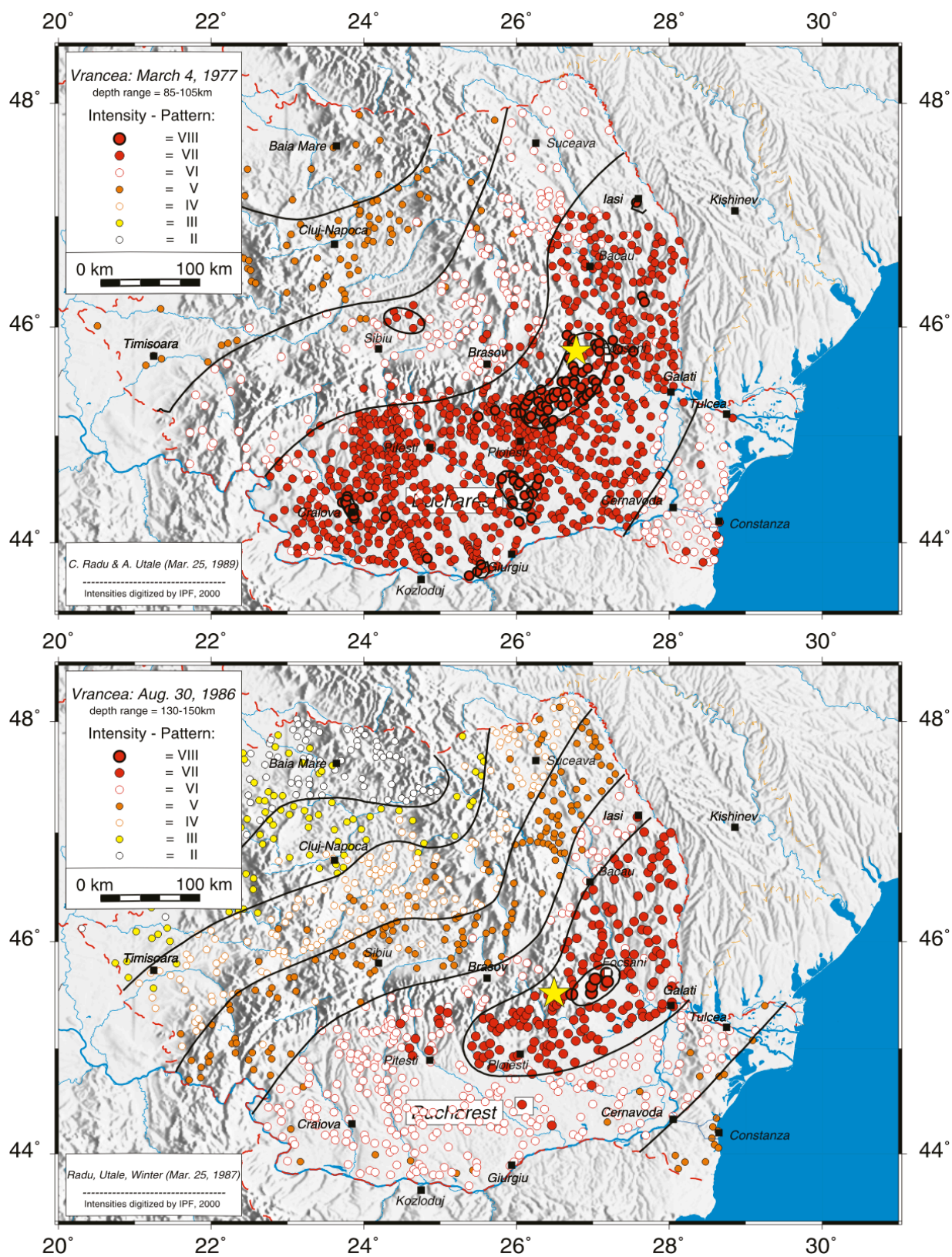


Figure 7

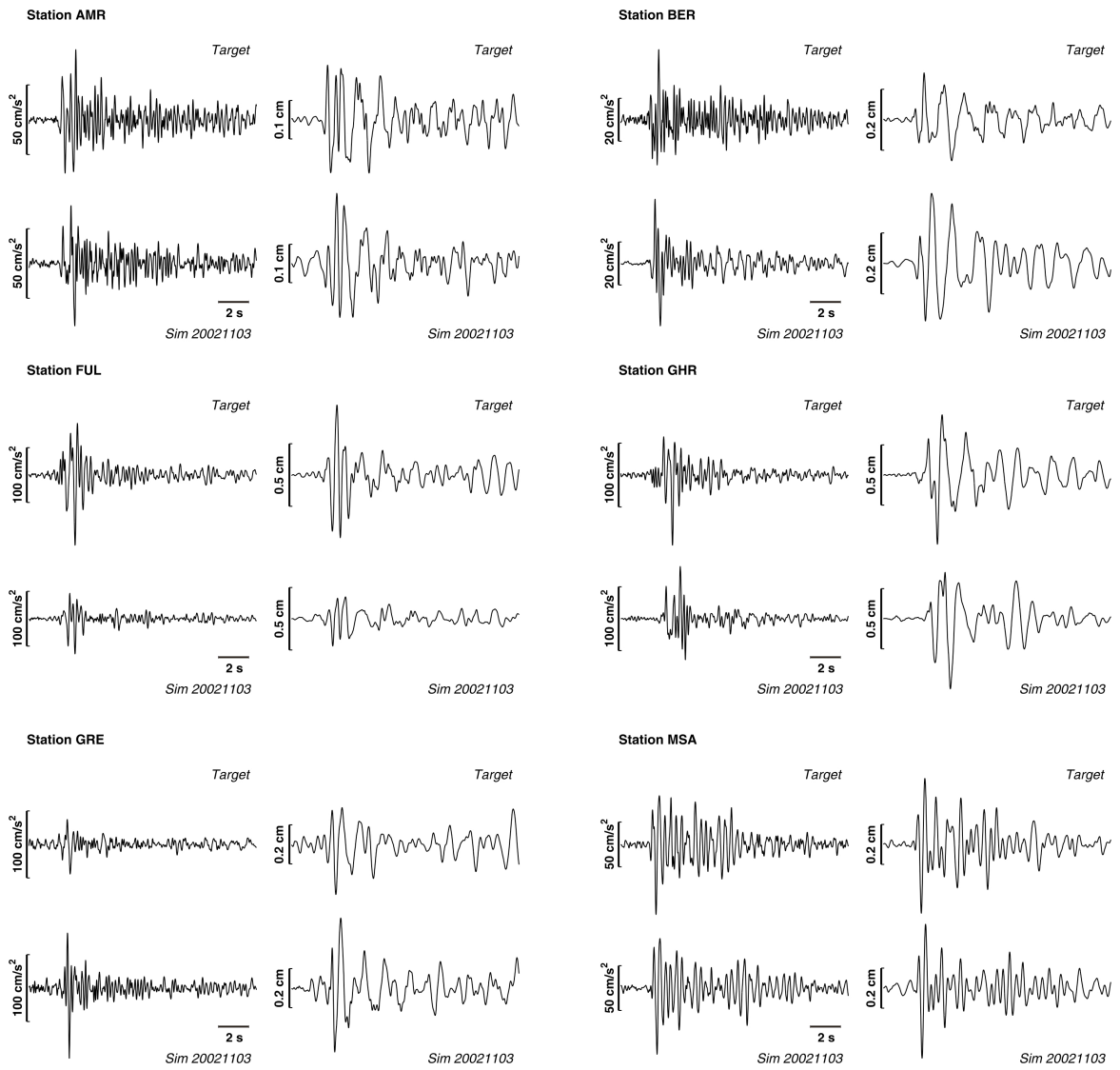


Figure 8

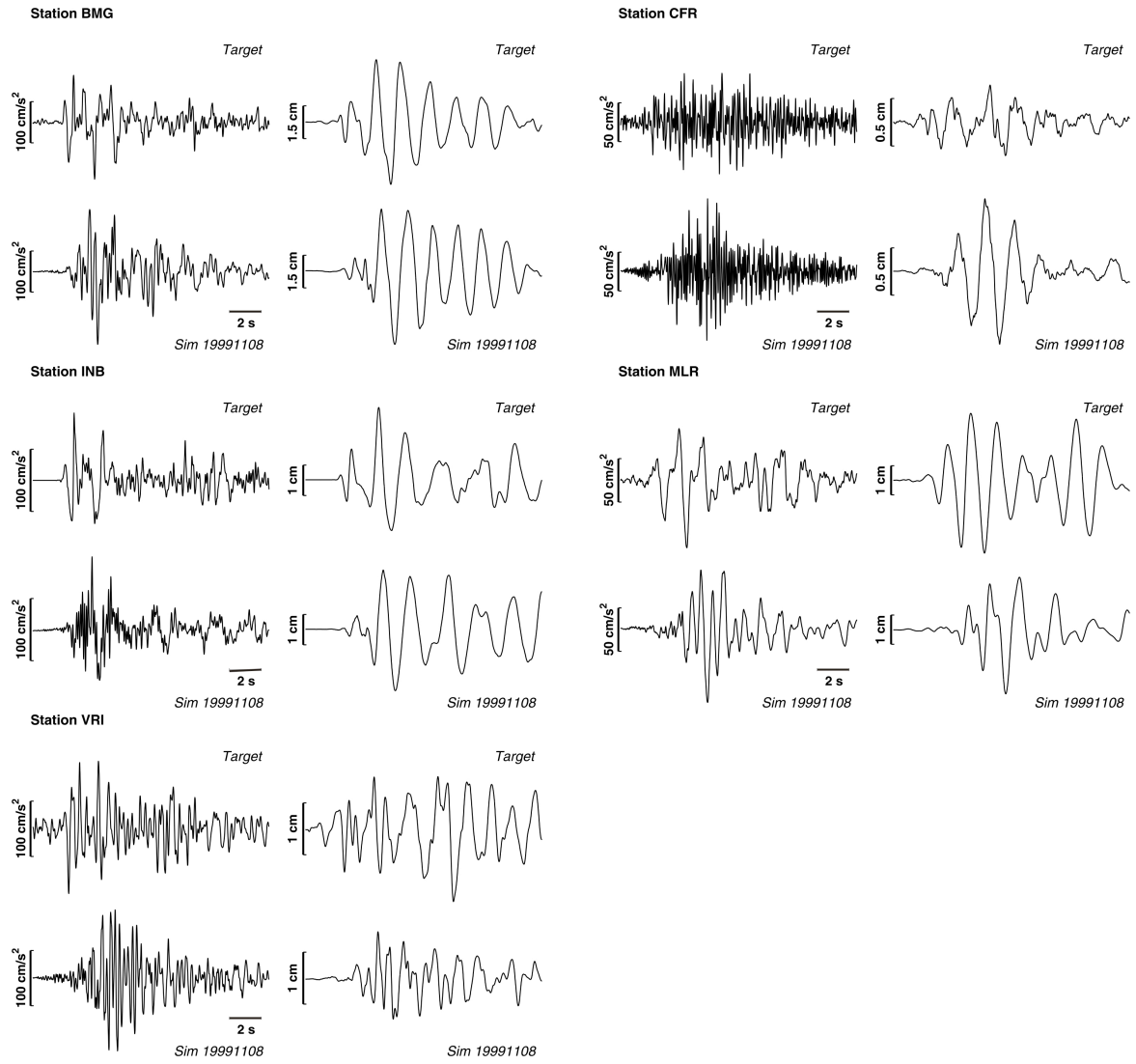


Figure 9

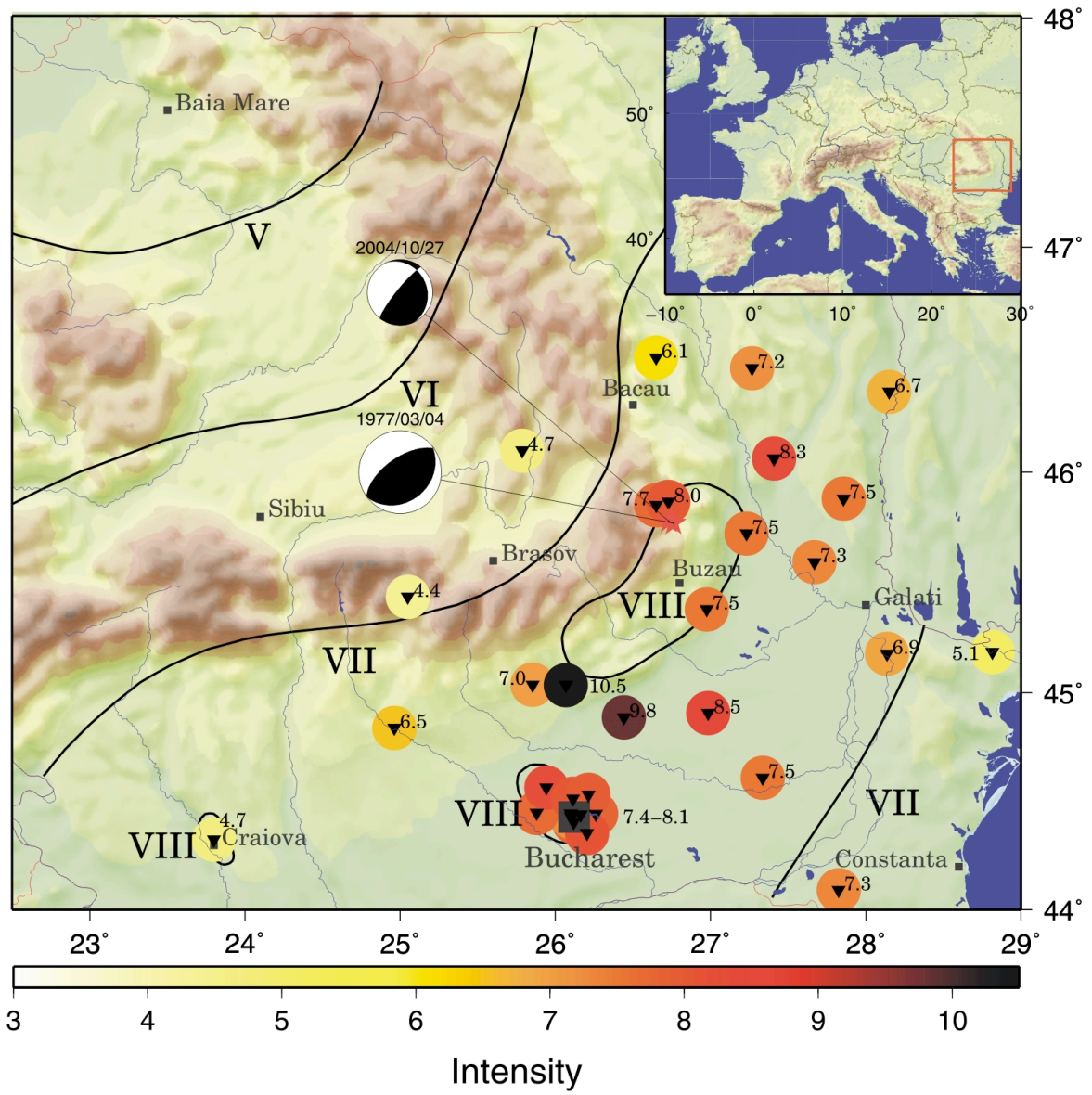
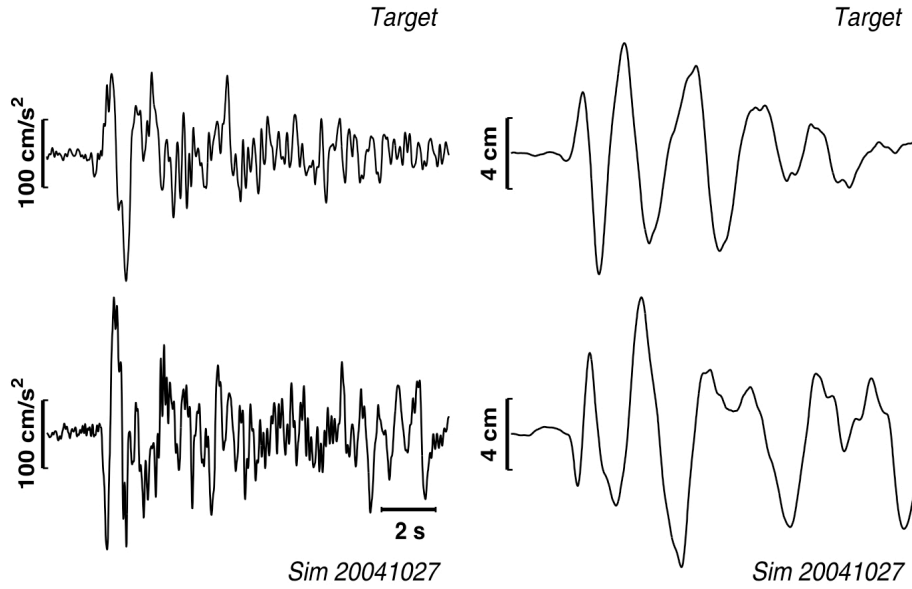


Figure 10

Station INB



Fourier Amplitude Spectrum at station INB

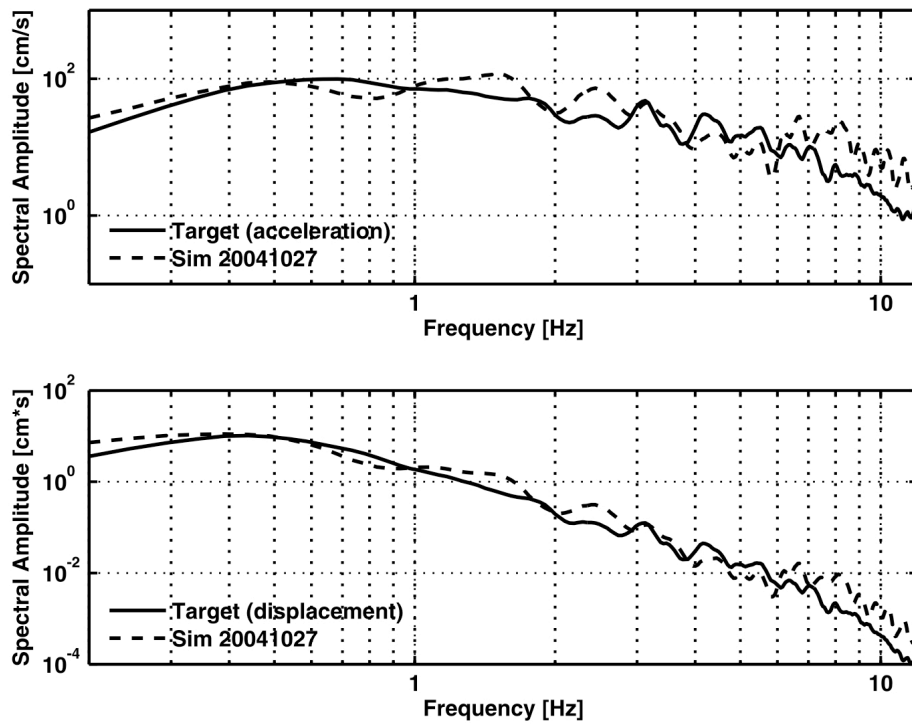


Figure 11

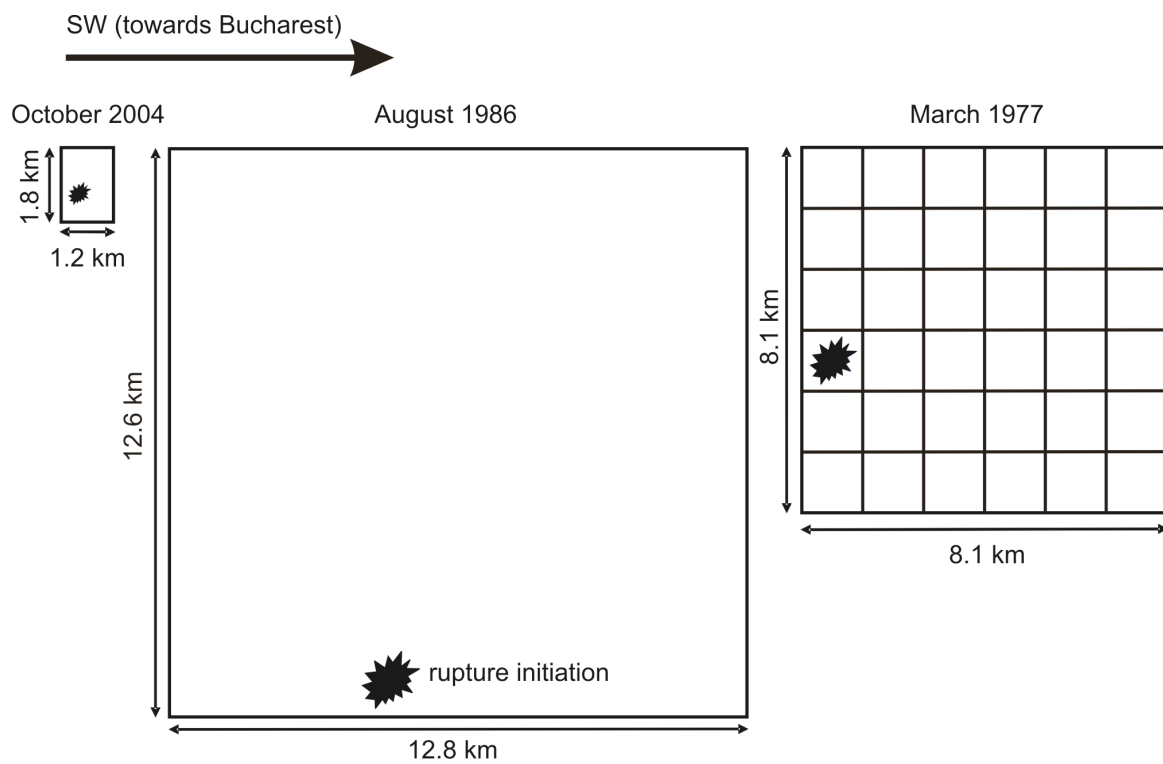


Figure 12